nature communications

Article

https://doi.org/10.1038/s41467-025-57728-3

Narrowed pore conformations of aquaglyceroporins AQP3 and GlpF

Received: 25 February 2024

Accepted: 27 February 2025

Published online: 20 March 2025

Check for updates

Daisuke Kozai[1], Masao Inoue[2], Shota Suzuki[1], Akiko Kamegawa[1,3], Kouki Nishikawa[3], Hiroshi Suzuki[1], Toru Ekimoto[2], Mitsunori Ikeguchi[2,4] & Yoshinori Fujiyoshi[1,3]

Aquaglyceroporins such as aquaporin−3 (AQP3) and its bacterial homologue GlpF facilitate water and glycerol permeation across lipid bilayers. X-ray crystal structures of GlpF showed open pore conformations, and AQP3 has also been predicted to adopt this conformation. Here we present cryo-electron microscopy structures of rat AQP3 and GlpF in different narrowed pore conformations. In *n*-dodecyl-β-D-maltopyranoside detergent micelles, aromatic/arginine constriction filter residues of AQP3 containing Tyr212 form a 2.8-Å diameter pore, whereas in 1-palmitoyl-2-oleoyl-sn-glycero-3-phosphocholine (POPC) nanodiscs, Tyr212 inserts into the pore. Molecular dynamics simulation shows the Tyr212-in conformation is stable and largely suppresses water permeability. AQP3 reconstituted in POPC liposomes exhibits water and glycerol permeability, suggesting that the Tyr212-in conformation may be altered during permeation. AQP3 Y212F and Y212T mutant structures suggest that the aromatic residue drives the pore-inserted conformation. The aromatic residue is conserved in AQP7 and GlpF, but neither structure exhibits the AQP3-like conformation in POPC nanodiscs. Unexpectedly, the GlpF pore is covered by an intracellular loop, but the loop is flexible and not primarily related to the GlpF permeability. Our findings illuminate the unique AQP3 conformation and structural diversity of aquaglyceroporins.

Water channels named aquaporins (AQPs) are membrane proteins that facilitate the permeation of water across lipid bilayers to the exclusion of ions and protons[1]. AQPs that permeate not only water but also small solutes such as glycerol are named aquaglyceroporins[1,2]. Thirteen human AQPs identified to date have different permeabilities and are mainly classified as follows: AQP0, AQP1, AQP2, AQP4, and AQP5 are considered water-selective type AQPs, while AQP3, AQP7, AQP9, and AQP10 are aquaglyceroporins[3,4]. AQPs are regulated by several factors, including pH, phosphorylation, and protein interactions[5–8]. Functionally different AQPs underlying various physiological and pathological phenomena are distinctly distributed in the body[1–8].

The permeability of AQPs is related to their channel pore properties. AQPs have a unique fold that forms a tetramer with one water-permeable pore per monomer[5,9,10]. The aromatic/arginine (ar/R) region located at the extracellular side of the channel pore forms a constriction filter[11,12]. While the arginine residue is highly conserved, the aromatic residues vary among AQPs[13]. The variety of ar/R filters relates to the different permeabilities of AQPs for water and solutes[11–17]. Below the ar/R filter, two half-membrane-spanning helices insert from both sides of the membrane and meet in the centre of the pore with a highly conserved asparagine-proline-alanine (NPA) motif[9]. The helical dipole moments of the short helices create a positive electrostatic field

[1]Cellular and Structural Physiology Laboratory (CeSPL), Advanced Research Initiative, Institute of Integrated Research, Institute of Science Tokyo, Tokyo, Japan. [2]Graduate School of Medical Life Science, Yokohama City University, Yokohama, Japan. [3]Joint Research Course for Advanced Biomolecular Characterization, Faculty of Agriculture, Tokyo University of Agriculture and Technology, Tokyo, Japan. [4]HPC- and AI-driven Drug Development Platform Division, Center for Computational Science, RIKEN, Yokohama, Japan. e-mail: yoshi.cesp@tmd.ac.jp

around the NPA motifs with the pore-facing asparagine residues[9]. These NPA motifs with an electrostatic field together with the ar/R filter are proposed to contribute to the permeabilities of AQPs without permeation of ions and protons[5,9,18–21].

Structural analyses of many water-selective AQPs and aquaglyceroporins have been performed by X-ray and electron crystallography, and single-particle cryo-electron microscopy (cryo-EM) analysis[22–24]. *Escherichia coli* (*E. coli*) GlpF was the first structurally determined aquaglyceroporin[10,21]. The mammalian aquaglyceroporin AQP7 structure has also been solved[25–27]. Expression of AQP7 in human pancreatic cells and its junction structure via extracellular loops were recently reported[28]. AQP10-specific low-pH dependent glycerol release from adipocytes was demonstrated by functional and structural analyses[29]. The regulatory features governing the structures and functions of other aquaglyceroporins, such as AQP3, however, remain unclear. A homology model of the AQP3 structure, in which the ar/R filter forms an open pore, has been used for in silico studies[30–33].

In this work, we perform cryo-EM structural analysis of rat AQP3, revealing two snapshots of AQP3: 1) ar/R filter forms a pore with a diameter of 2.8 Å, and 2) a previously unobserved narrowed pore conformation in which Tyr212, an aromatic residue of the ar/R filter, inserts into the pore. All-atom molecular dynamics (MD) simulations show that the AQP3 Tyr212-in conformation is stable and largely suppresses water permeability. AQP3 Y212F and Y212T mutant structures show that the pore-inserted conformation is due to the aromatic residue. Aquaglyceroporins AQP7 and GlpF contain Tyr223 and Phe200, respectively, at the site of Tyr212 in AQP3, yet neither structure exhibits the AQP3-like narrowed pore conformation. Unexpectedly, the cryo-EM structure of GlpF reveals a narrowed pore by the intracellular loop, similar to conformations observed in plant AQPs. Structural model B-factor suggests that the intracellular loop is relatively flexible. MD simulations support that the GlpF intracellular loop is flexible allowing water to pass through the region near the loop. Our study elucidates the structural variety of aquaglyceroporins.

Results

Structures of AQP3 in DDM micelles and in POPC or DMPC nanodiscs

To experimentally determine the structure of AQP3, we expressed rat AQP3 in insect cells and purified it using the detergent *n*-dodecyl-β-D-maltopyranoside (DDM) (Supplementary Fig. 1a, b). AQP3 was reconstituted into lipid nanodiscs[34] by mixing DDM-solubilised AQP3 with MSP proteins and 1-palmitoyl-2-oleoyl-sn-glycero-3-phosphocholine (POPC), followed by the application of Bio-Beads to remove the DDM (Supplementary Fig. 1a, b). Cryo-EM maps of AQP3 in DDM micelles and in POPC nanodiscs (hereafter referred to as $AQP3^{DDM}$ and $AQP3^{POPC}$, respectively) were obtained at resolutions of 3.12 Å and 2.94 Å, respectively (Fig. 1a, b and Supplementary Figs. 2 and 3a, b). As expected, AQP3 forms a tetrameric aquaporin fold (Fig. 1c). The monomer consists of six transmembrane helices (H1–H6) with intracellular N- and C-termini and five loop regions (loop A–E), of which intracellular loop B and extracellular loop E contain reentrant loops with short helices (HB and HE) that feature NPA motifs (Fig. 1d).

Importantly, AQP3 exhibits significantly different conformations between structures in DDM micelles and POPC nanodiscs. The ar/R filter formed by Phe63, Tyr212, and Arg218 of $AQP3^{DDM}$ creates a pore diameter of 2.8 Å (Tyr212-out conformation; Fig. 1e and Supplementary Fig. 4a). For $AQP3^{POPC}$, however, a conformational change of extracellular reentrant loop E is observed with Tyr212 inserted into the pore (Tyr212-in conformation; Fig. 1f). The pore of $AQP3^{POPC}$ is calculated to be occluded by this conformational change (Supplementary Fig. 4b). Tyr212 inserts into the centre of the pore near the NPA motifs, and the hydroxyl group of Tyr212 forms a hydrogen bond contact with Asn83 in the NPA motif of HB (Fig. 1g, left panel). The inserted Tyr212 on reentrant loop E pushes Phe63 outward at the ar/R filter (Fig. 1g, right panel). The reentrant loop E of $AQP3^{POPC}$ is kinked at Gly207 with a large conformational change compared with that of $AQP3^{DDM}$ (Fig. 1g, left panel). While the observed density map at the pore of $AQP3^{POPC}$ largely corresponds to Tyr212, that at the pore of $AQP3^{DDM}$ appears as a relatively continuous shape (Fig. 1h, i). It was difficult to assign a specific model in the density map at the pore of $AQP3^{DDM}$ (Fig. 1h).

Some additional differences were observed between the structures of $AQP3^{DDM}$ and $AQP3^{POPC}$. Along with the loop E conformational changes in $AQP3^{POPC}$, Phe56 at the extracellular side of the H2 helix flips upward and His53 at the adjacent monomer's loop A becomes disordered (Supplementary Fig. 5a, b). In addition, the loop C residues His154 and Leu155 are also conformationally changed in $AQP3^{POPC}$ (Supplementary Fig. 5a, b). Furthermore, the position of the intracellular loop D shifts to the pore side in $AQP3^{POPC}$ compared with $AQP3^{DDM}$ (Fig. 1e, f and Supplementary Fig. 5c).

We measured the phospholipid contents in the purified proteins of $AQP3^{DDM}$ and $AQP3^{POPC}$. Phospholipids were detected in $AQP3^{DDM}$ samples to a lesser extent than in $AQP3^{POPC}$ (Supplementary Fig. 6a), suggesting that native phospholipids from insect cells are not completely stripped away by DDM solubilisation. The shapes and sizes of the cryo-EM maps around the tetrameric proteins differ between $AQP3^{DDM}$ and $AQP3^{POPC}$ (Supplementary Fig. 6b,c). These cryo-EM maps may correspond to DDM or surrounding lipids, but it was difficult to assign specific models.

The structure of AQP3 in 1,2-dimyristoyl-sn-glycero-3-phosphocholine (DMPC) nanodiscs (referred to as $AQP3^{DMPC}$) was also solved (Supplementary Figs. 1c, d and 3c). $AQP3^{DMPC}$ particles appeared as oval discs under the cryo-EM analysis without symmetry application (Supplementary Fig. 7a). All four monomers of $AQP3^{DMPC}$ exhibited the Tyr212-in conformation like $AQP3^{POPC}$ (Supplementary Fig. 7b). Cryo-EM maps like acyl chains of lipids were observed around some monomers of $AQP3^{DMPC}$ (Supplementary Fig. 7c).

MD simulations of the AQP3 Tyr212-out and Tyr212-in conformations

To examine structural stability and water distribution in the Tyr212-out and Tyr212-in conformations of AQP3, 500-ns MD simulations were conducted. The Tyr212-out conformation was observed in the purified protein of $AQP3^{DDM}$, which contains not only DDM but also phospholipids (Supplementary Fig. 6a). The Tyr212-out conformation was examined in MD simulations both in DDM micelles and POPC bilayers to investigate the effects of surrounding environments. The Tyr212-in conformation was also examined in the same manner. The four systems were generated by burying the AQP3 tetramers of the Tyr212-out and Tyr212-in conformations in DDM micelles and POPC bilayers as follows: the modelled AQP3 tetramer of the Tyr212-out conformation in DDM micelles (referred to as $I_{Tyr212\text{-}out/DDM}$ hereafter); that of the Tyr212-out conformation in the POPC bilayer ($I_{Tyr212\text{-}out/POPC}$); that of the Tyr212-in conformation in DDM micelles ($I_{Tyr212\text{-}in/DDM}$); and that of the Tyr212-in conformation in the POPC bilayer ($I_{Tyr212\text{-}in/POPC}$). These systems were used in MD simulations (Supplementary Fig. 8a–d and Supplementary Movies 1–4). The overall structures were not denatured during the MD simulations (Supplementary Fig. 8e). In the MD simulations for $I_{Tyr212\text{-}out/DDM}$ and $I_{Tyr212\text{-}in/DDM}$, the dissociation of DDM molecules from the micelle was not observed, indicating that the system setup for DDM micelles is appropriately adjusted.

The distance between Tyr212 and Asn83 for each chain of the tetramers was monitored during the MD trajectories (Fig. 2a–f). In the simulation of the Tyr212-out conformation, the Tyr212–Asn83 distance for $I_{Tyr212\text{-}out/DDM}$ decreased from 12.3 Å in the initial structure to ~6 Å at two chains of the tetramer, and that for $I_{Tyr212\text{-}out/POPC}$ decreased to ~6 Å at two chains and decreased further to ~4 Å at one chain (Fig. 2a–c). In contrast, the Tyr212–Asn83 distance for $I_{Tyr212\text{-}in/DDM}$ and $I_{Tyr212\text{-}in/POPC}$ were maintained at ~4 Å during the simulations except for one chain of $I_{Tyr212\text{-}in/DDM}$, in which the distance became ~7 Å during the last 30 ns

https://doi.org/10.1038/s41467-025-57728-3

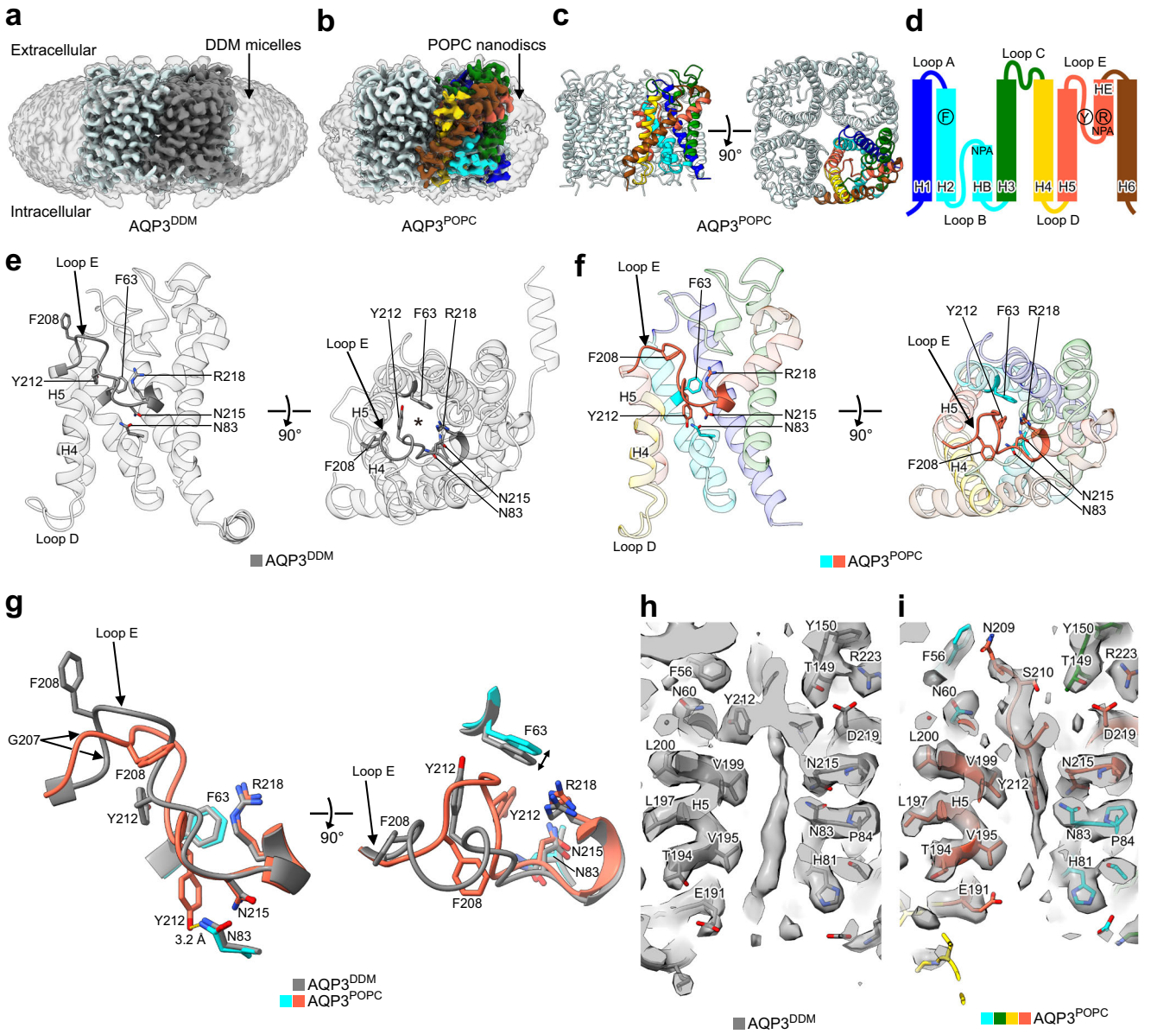

Fig. 1 | Conformational differences between AQP3 in DDM micelles and AQP3 in POPC nanodiscs. Cryo-EM maps of AQP3^{DDM} (**a**) and AQP3^{POPC} (**b**). Regions of micelles and nanodiscs are shown as transparent using unsharpened maps. The monomers of AQP3^{DDM} and AQP3^{POPC} are highlighted in gray and rainbow colours, respectively. **c** The tetrameric modelled structure of AQP3^{POPC} shown as a ribbon representation from the side and extracellular views. **d** Schematic topology of an AQP3 monomer coloured as in (**b**, **c**). The NPA motifs at the HB and HE short helices are indicated as NPA. The ar/R filter residues, Phe63 at H2, Tyr212 at reentrant loop E, and Arg218 at HE, are indicated as F, Y, and R, respectively. Overall structures of the monomers of AQP3^{DDM} (**e**) and AQP3^{POPC} (**f**) from the side and extracellular views. The reentrant loop E, ar/R filter residues, and asparagines at the NPA motifs are highlighted with several residues shown as sticks. The channel pore of the AQP3^{DDM} monomer is indicated by an asterisk from the extracellular view (**e**, right panel). For clarity, loop B, loop C, and H6 are partially removed from the side views. **g** Superimposition of the regions around reentrant loop E of AQP3^{DDM} and AQP3^{POPC} from the side and extracellular views. The movement of Phe63 is indicated by a two-way arrow (right panel). The hydrogen bond between Tyr212 and Asn83 of AQP3^{POPC} is indicated by a yellow dotted line (left panel). Cryo-EM maps and models of the pore regions of the monomers of AQP3^{DDM} (**h**) and AQP3^{POPC} (**i**).

(Fig. 2d–f). These results showed that the Tyr212-out conformation is relatively flexible and that the flexibility is independent of the surrounding environments of DDM micelles and POPC bilayers. These results also showed that the inserted Tyr212 is stable in both DDM micelles and POPC bilayers. The fluctuations observed by MD simulations in the reentrant loop E of the Tyr212-out conformations were larger than those of the Tyr212-in conformations (Supplementary Fig. 8f). The experimental structural flexibility of the reentrant loop E represented by the B-factor of cryo-EM structure of AQP3^{DDM} was smaller than that of AQP3^{POPC} (Supplementary Fig. 8g). The stability of the reentrant loop E represented by the B-factor of AQP3^{DDM} was inconsistent with fluctuations observed in the Tyr212-out conformations by MD simulations (Supplementary Fig. 8f, g).

The water distribution in the AQP3 pores was calculated from the obtained MD trajectories. In calculating the water distribution, the number of water molecules in the pore axis was counted and averaged over the four pores of a tetramer and over all snapshots of the simulations (Fig. 2g). For $I_{Tyr212\text{-}in/DDM}$ and $I_{Tyr212\text{-}in/POPC}$, the relative density of the water molecules equalled almost zero along the pore axis, spanning a distance of 2 to 8 Å, which is near the region of the inserted Tyr212 (Fig. 2g). Furthermore, the water permeability in the MD simulations was also measured by counting how many water

https://doi.org/10.1038/s41467-025-57728-3

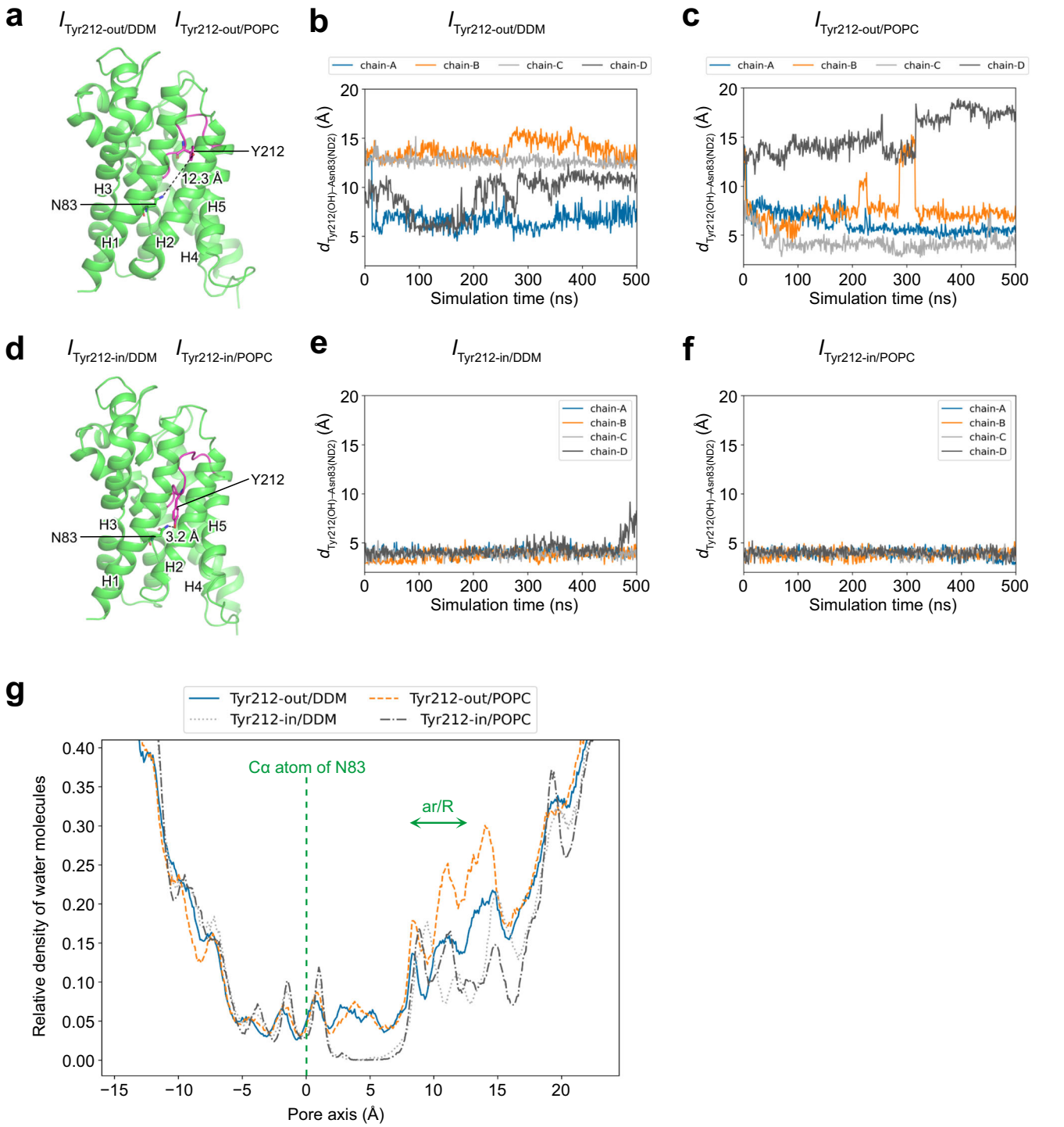

Fig. 2 | MD simulations for the Tyr212-out and Tyr212-in conformations of AQP3. Initial and monitored distance between Tyr212(OH) and Asn83(ND2) in MD simulations for the AQP3 Tyr212-out (**a**–**c**) and Tyr212-in (**d**–**f**) conformations. The monitored distances are shown for $I_{Tyr212\text{-}out/DDM}$ (**b**), $I_{Tyr212\text{-}out/POPC}$ (**c**), $I_{Tyr212\text{-}in/DDM}$ (**e**), and $I_{Tyr212\text{-}in/POPC}$ (**f**). In the graphs of the monitored distance, the plots of the four chains of tetramers are shown (**b**, **c**, **e**, **f**). The reentrant loop E is represented by magenta (**a**, **d**). **g** Water distribution in pores during MD simulations for four systems. The pore axes are aligned with *z*-axes of the cryo-EM structures. The origin of the pore axis is set at the *z*-coordinate of the Cα atom of Asn83.

molecules passed through the four pores in the intracellular or extracellular direction. The total number of water molecules passing through was 1989 for $I_{Tyr212\text{-}out/DDM}$, 1251 for $I_{Tyr212\text{-}out/POPC}$, 75 for $I_{Tyr212\text{-}in/DDM}$, and 5 for $I_{Tyr212\text{-}in/POPC}$. Water molecule orientations in the pore were also analysed. Water molecules are oriented in opposite directions in the two regions of the AQP3 pore separated by the NPA motif (Supplementary Fig. 8h). This finding is consistent with a previous report showing water molecule orientations in the GlpF pore[21].

The essential findings from the MD simulations of AQP3 are the differences in structural stability and water permeability between Tyr212-out and Tyr212-in conformations. All-atom conventional MD was chosen as the method because the two conformations are quite

similar except for loop E and large structural changes of a membrane protein are not focused on in this study. The results are based on the behaviours of the four chains in the AQP3 tetramer. In the analyses in the monomer unit, one MD trajectory of the tetramer can be considered to include four independent trajectories of the four chains. The four chains had different initial conformations and velocities of atoms in the production run because of the energy minimisation and equilibration runs before it. In the MD simulations for the Tyr212-out conformation, the Tyr212–Asn83 distance changed in some chains in the timescale of tens of nanoseconds (see Fig. 2b, c). Also, the differences in water distribution and in number of permeations were captured within a sampling range of 500 ns. Therefore, the simulation length appeared to be sufficient for the analyses of structural stability and water permeability focused on in this study.

Aromatic residue required for the pore insertion of AQP3 in POPC nanodiscs

To investigate the mechanism of the pore insertion observed in AQP3^{POPC}, Y212F and Y212T mutants were constructed. The Y212F mutation lacks the hydroxyl group but retains the aromatic ring. The Y212T mutation lacks the aromatic ring. We expressed and purified AQP3 Y212F and Y212T mutants (Supplementary Fig. 1e, f). We obtained their cryo-EM structures in POPC nanodiscs (hereafter referred to as AQP3-Y212F^{POPC} and AQP3-Y212T^{POPC}, respectively; Supplementary Fig. 3d, e). The structure of AQP3-Y212F^{POPC} exhibited conformational changes of the reentrant loop E with the pore insertion of Y212F near the NPA motifs, similar to AQP3^{POPC} (Fig. 3a). On the other hand, the structure of AQP3-Y212T^{POPC} revealed that Y212T does not insert into the pore, but covers the pore (Fig. 3b). The cryo-EM map corresponding to reentrant loop E residues from Gly207 to Thr212 of AQP3-Y212T^{POPC} is more disordered than that of the wild-type AQP3^{POPC} and AQP3-Y212F^{POPC} (Fig. 3c–e). The unsharpened map of AQP3-Y212T^{POPC} supports that the reentrant loop E of AQP3-Y212T^{POPC} appears to cover the pore (Fig. 3e) and the position of Phe208 in AQP3-Y212T^{POPC} differs from the position of Phe208 in AQP3^{POPC} and AQP3-Y212F^{POPC} (Fig. 3e). The pore of AQP3-Y212F^{POPC} is occluded like that of AQP3^{POPC} (Supplementary Fig. 4b). The pore diameter of AQP3-Y212T^{POPC} was calculated to be wider than that of AQP3^{POPC} and AQP3-Y212F^{POPC} (Supplementary Fig. 4b). These results suggest that an aromatic residue (Tyr or Phe) is necessary for the pore insertion of AQP3 in POPC nanodiscs.

To evaluate whether or not the structural instability of the reentrant loop E of AQP3-Y212T^{POPC} appears in DDM micelles, structural analysis of AQP3 Y212T in DDM micelles (hereafter referred to as AQP3-Y212T^{DDM}) was performed (Supplementary Fig. 3f). Reentrant loop E residues are not disordered in the cryo-EM structure of AQP3-Y212T^{DDM} similar to those of AQP3^{DDM} (Fig. 3f–h). Cryo-EM maps that might correspond to DDM or lipids appear around tetrameric AQP3-Y212T^{DDM} and are not the same as those in AQP3-Y212F^{POPC} and AQP3-Y212T^{POPC} (Supplementary Fig. 6d–f).

The structure of AQP3-Y212T^{DDM} exhibited two additional features at the pore. First, the Y212T mutation changes the position of reentrant loop E to narrow the pore around Y212T compared with that in AQP3^{DDM} (Fig. 3g, h and Supplementary Fig. 4a). Second, the cryo-EM map at the channel pore of AQP3-Y212T^{DDM} shows a clear density at the intracellular side, matching that in DDM (Fig. 3i). Such a clear shape is not observed in the cryo-EM maps of the AQP3-Y212F^{POPC} and AQP3-Y212T^{POPC} pores (Supplementary Fig. 9a, b).

Water and glycerol permeability of AQP3 and its mutants in POPC liposomes

Proteoliposomes were made by DDM-solubilised proteins and POPC to evaluate the water and glycerol permeability using a stopped-flow apparatus. We compared the protein and phospholipid contents of proteoliposomes among AQP3 wild-type, Y212F, and Y212T (Supplementary Fig. 9c and Supplementary Table 1). We confirmed that these prepared proteoliposomes exhibits similar protein/phospholipid weight ratios (Fig. 4a).

AQP3 proteoliposomes shrank faster than empty liposomes under hyperosmotic conditions, indicating the water permeability of the reconstituted AQP3 in proteoliposomes (Fig. 4b, c and Supplementary Table 1). Both AQP3 Y212F and Y212T mutants also exhibited water permeability, and the permeability of AQP3 Y212T is slightly faster than that of AQP3 wild-type and significantly faster than that of Y212F (Fig. 4b, c and Supplementary Table 1). AQP3 also exhibited glycerol permeability under glycerol gradient conditions (Fig. 4d, e and Supplementary Table 1). Both AQP3 Y212F and Y212T mutants exhibited glycerol permeability, with Y212T exhibiting significantly faster glycerol permeability than AQP3 wild-type and Y212F (Fig. 4d, e and Supplementary Table 1).

Structure of AQP7 in POPC nanodiscs

We focused on the sequence conservation of Tyr212 in AQP3 among human AQPs. Only AQP7, an aquaglyceroporin, has an aromatic residue, Tyr223 (Fig. 5a). The cryo-EM structure of human AQP7 in detergent micelles using glyco-diosgenin was recently reported[28]. Therefore, we purified and performed cryo-EM structural analysis of human AQP7 only in POPC nanodiscs (termed AQP7^{POPC}; Supplementary Figs. 1g, h and 3g). AQP7^{POPC} did not exhibit the narrowed pore conformation like AQP3^{POPC}, despite the presence of aromatic residues at reentrant loop E (Fig. 5b and Supplementary Fig. 10a). The structure of AQP7^{POPC} is similar to that of AQP7 in detergent micelles[28] (Fig. 5b). The positions of the ar/R filter residues and reentrant loop E are similar between AQP7^{POPC} and AQP3^{DDM} (Supplementary Fig. 11a).

We prepared AQP7 reconstituted POPC liposomes. We confirmed the protein contents (Supplementary Fig. 11b, c and Supplementary Table 1), water permeability (Supplementary Fig. 11d, e and Supplementary Table 1), and glycerol permeability (Supplementary Fig. 11f, g and Supplementary Table 1) of reconstituted AQP7.

Structures of GlpF in DDM micelles and POPC nanodiscs

Sequence analysis showed that *E. coli* GlpF also has an aromatic residue, Phe200, at the same position as Tyr212 in AQP3 (Fig. 5a). Therefore, we purified and performed cryo-EM structural analyses of GlpF in DDM micelles and POPC nanodiscs (termed GlpF^{DDM} and GlpF^{POPC}, respectively; Supplementary Figs. 1i, j, 3h, i, and 12a). GlpF^{POPC} did not exhibit the narrowed pore conformation like AQP3^{POPC}, despite the presence of an aromatic residue at reentrant loop E (Fig. 5c and Supplementary Fig. 10b). A structural model of GlpF^{DDM} was not constructed because of the relatively low-resolution map, but the model of the reentrant loop E of GlpF^{POPC} fits well to the cryo-EM map of GlpF^{DDM} (Fig. 5d), indicating the same conformation of loop E between GlpF^{DDM} and GlpF^{POPC}. The residues at the ar/R filter of AQP7 and AQP3 are the same, but differ from those of GlpF as follows: Trp48 in GlpF corresponds to Phe63 in AQP3 and Phe74 in AQP7, and Phe200 in GlpF corresponds to Tyr212 in AQP3 and Tyr223 in AQP7 (Fig. 5a). The positions of the ar/R filter residues and reentrant loop E are similar between GlpF^{POPC} and AQP3^{DDM} (Supplementary Fig. 12b).

Notably, GlpF^{POPC} exhibits a previously unobserved structure where the pore is covered by loop D on the intracellular side (Fig. 5c). The cryo-EM map of GlpF^{DDM} also shows that the intracellular side of the pore is covered by loop D (Fig. 5e), indicating that this is not dependent on the DDM or POPC nanodisc environment. Loop D of GlpF^{POPC} mainly faces the pore with its Val173 (Fig. 5c). While the residue corresponding to Val173 in GlpF is also a valine (Val186) in AQP3 (Fig. 5a), loop D does not cap the pore of AQP3^{POPC} (Fig. 5f). Comparison of the structure and sequence suggests that the inserted proline residue found only in GlpF, Pro177, generates the differences (Fig. 5a, f). The GlpF ΔP177 mutant in POPC nanodiscs (termed as GlpF-

https://doi.org/10.1038/s41467-025-57728-3

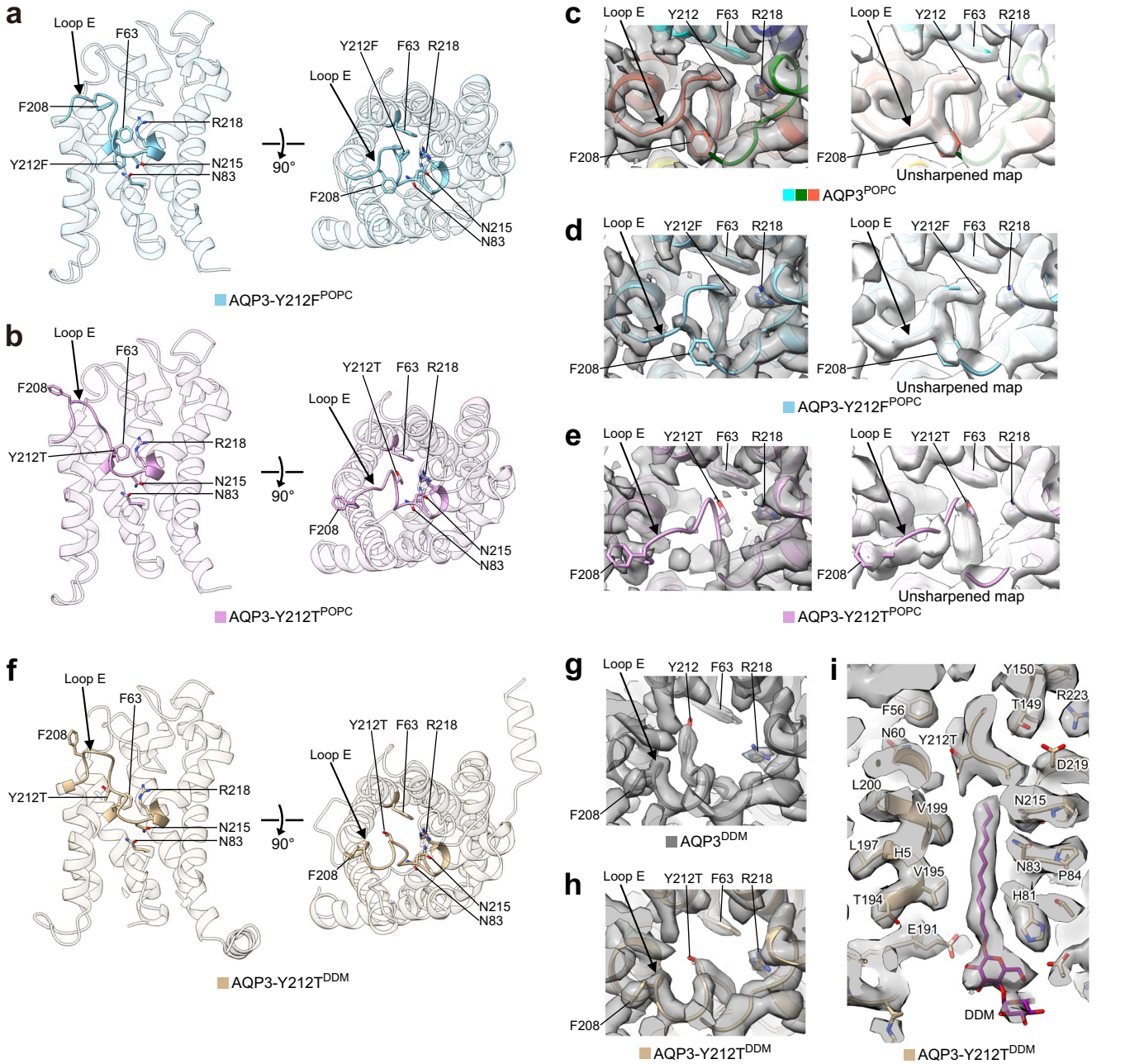

Fig. 3 | Structures of AQP3 Y212F and Y212T mutants. Overall structures of the monomers of AQP3-Y212F^{POPC} (**a**) and AQP3-Y212T^{POPC} (**b**) from the side and extracellular views. The reentrant loop E, ar/R filter residues, and asparagines at the NPA motifs are highlighted with several residues shown as sticks. For clarity, loop B, loop C, and H6 are partially removed from the side views. Extracellular views of cryo-EM maps and models around loop E regions of AQP3^{POPC} (**c**), AQP3-Y212F^{POPC} (**d**), and AQP3-Y212T^{POPC} (**e**). Unsharpened maps are also presented (right panel). **f** Overall structure of the monomer of AQP3-Y212T^{DDM} shown as in (**a**, **b**). Modelled DDM is not shown. Extracellular views of cryo-EM maps and models around loop E regions of AQP3^{DDM} (**g**) and AQP3-Y212T^{DDM} (**h**). **i** Enlarged side view of cryo-EM map and model of pore region of AQP3-Y212T^{DDM} with modelled DDM molecule coloured purple.

ΔP177^{POPC}) was purified and subjected to cryo-EM structural analysis (Supplementary Figs. 1k, l, 3j, and 12c). The intracellular loop D of GlpF-ΔP177^{POPC} predictably does not cover the pore (Fig. 5g and Supplementary Fig. 10b). The C-terminus also shows a different conformation between GlpF^{POPC} and GlpF-ΔP177^{POPC} (Fig. 5h). GlpF-ΔP177^{POPC} is modelled up to Gly256, but GlpF^{POPC} is modelled up to Cys261.

Loop D does not cap the pore and the C-terminus shows a different conformation in the X-ray crystal structure of GlpF without glycerol[21] compared with GlpF^{POPC} (Supplementary Fig. 10b and 12d). The positions of loop D and the C-terminus of GlpF-ΔP177^{POPC} are more similar to those of the X-ray crystal structure of GlpF (Supplementary Fig. 12e).

The pore closure structures by loop D have been reported in other X-ray crystal structures of two plant AQPs, spinach PIP2;1 (SoPIP2;1)[35] and *Oryza sativa* NIP2;1 (OsNIP2;1)[36]. We compared the structures of SoPIP2;1 and OsNIP2;1 with GlpF^{POPC} (Supplementary Fig. 12f, g). The position of loop D in GlpF^{POPC} is not the same as that in SoPIP2;1 and OsNIP2;1.

MD simulations and permeability assays of GlpF and its mutant

In the same manner, as for AQP3, 500-ns MD simulations were conducted to examine the structural stability and water distribution of GlpF wild-type and GlpF ΔP177 in POPC bilayers. Modelling the tetramers of GlpF based on the cryo-EM structures of GlpF^{POPC} and GlpF-

https://doi.org/10.1038/s41467-025-57728-3

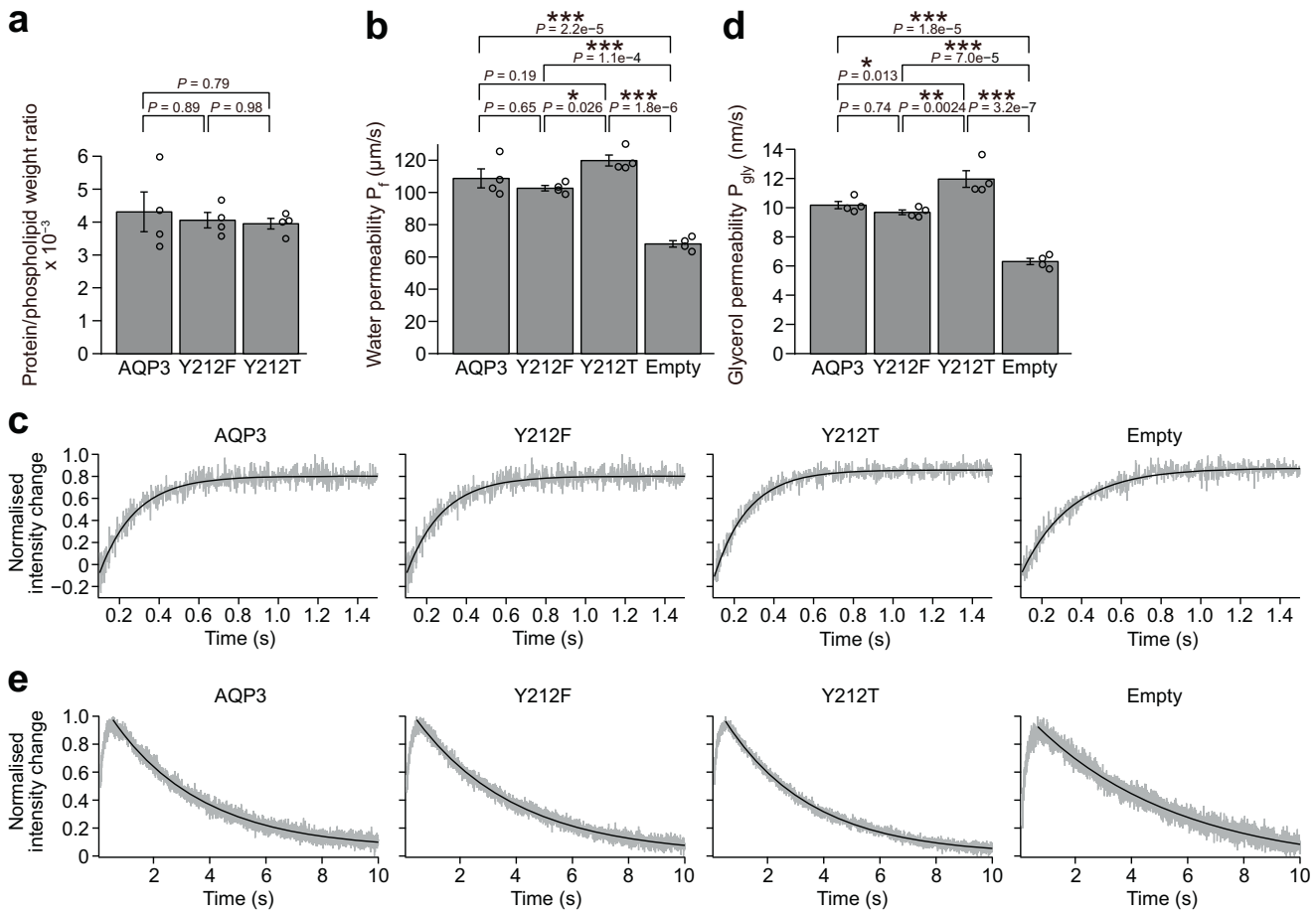

Fig. 4 | Stopped-flow measurements of AQP3 and mutants. a The measured protein/phospholipid weight ratio of AQP3, AQP3 Y212F, and AQP3 Y212T proteoliposomes. Averaged values ± SEM and individual data points are plotted ($n = 4$ independently reconstituted liposome samples from the same purified proteins). Data are statistically analysed using multiple comparison Tukey test. *P* values are indicated. **b**, **c** Stopped-flow measurements under NaCl hyperosmotic conditions for AQP3, AQP3 Y212F, and AQP3 Y212T proteoliposomes and empty liposomes. Averaged water permeability P_f values ± SEM and individual data points are plotted ($n = 4$ independently reconstituted liposome samples from the same purified proteins) (**b**). Data are statistically analysed using multiple comparison Tukey test. *P* values are indicated. $^*P < 0.05$ and $^{***}P < 0.001$. Representative time courses of normalised intensity change and fitted curves are shown (**c**). **d**, **e** Stopped-flow measurements under glycerol gradient conditions for AQP3, AQP3 Y212F, and AQP3 Y212T proteoliposomes and empty liposomes. Averaged glycerol permeability P_{gly} values ± SEM and individual data points are plotted ($n = 4$ independently reconstituted liposome samples from the same purified proteins) (**d**). Data are statistically analysed using multiple comparison Tukey test. *P* values are indicated. $^*P < 0.05$, $^{**}P < 0.01$, and $^{***}P < 0.001$. Representative time courses of normalised intensity change and fitted curves are shown (**e**). Source data are provided as a Source Data file.

ΔP177^{POPC}, the initial structures were generated by burying the tetramers in POPC bilayers. The two systems are referred as $I_{GlpF/POPC}$ and $I_{GlpF\text{-}\Delta P177/POPC}$ hereafter, and were used in the MD simulations (Supplementary Fig. 13a, b and Supplementary Movies 5 and 6). The overall structures of $I_{GlpF/POPC}$ and $I_{GlpF\text{-}\Delta P177/POPC}$ from Ser5 to Gly256 were not denatured during the MD simulations (Supplementary Fig. 13c). The C-terminus Arg257 to Cys261 of $I_{GlpF/POPC}$ fluctuated quite a bit in the MD simulations (Supplementary Fig. 13c).

The distances Val173–Ala79 and Gly170–Ala79 for each chain of the tetramers of $I_{GlpF/POPC}$ were monitored during the MD trajectory (Fig. 6a–d). The distance Val173–Ala79 moved with an amplitude of ~3 Å (Fig. 6a, b), and the distance Gly170–Ala79 moved more than that of Val173–Ala79 (Fig. 6c, d). The snapshot of loop D of $I_{GlpF/POPC}$ during the MD simulation showed that the position of loop D changed and water passed through near the loop D (Fig. 6e). The distance Val173–Ala79 for each chain of the tetramers in $I_{GlpF\text{-}\Delta P177/POPC}$ was monitored during the MD trajectory (Fig. 6f, g). The distance Val173–Ala79 moved with an amplitude of ~5 Å (Fig. 6f, g). The loop D of $I_{GlpF\text{-}\Delta P177/POPC}$ maintained its position away from the pore. The fluctuation of loop D in $I_{GlpF/POPC}$ was larger than that in $I_{GlpF\text{-}\Delta P177/POPC}$ (Supplementary Fig. 13d). The fluctuations observed in the loop D of GlpF wild-type and GlpF ΔP177 were consistent with the experimental structural flexibilities represented by the B-factor of cryo-EM structures of GlpF^{POPC} and GlpF-ΔP177^{POPC} (Supplementary Fig. 13e).

Water distribution in the GlpF pores was calculated in the same manner as that in AQP3 (Fig. 6h). The relative density of water molecules in $I_{GlpF/POPC}$ was lower than that in $I_{GlpF\text{-}\Delta P177/POPC}$ within the pore axis range of −15 to −5 Å, where the pore is capped by loop D, but it was not close to zero (Fig. 6h). The total number of passed water molecules in the MD simulations was 1132 for $I_{GlpF/POPC}$ and 2867 for $I_{GlpF\text{-}\Delta P177/POPC}$. Water molecule orientation in the pore was also analysed. Water molecules are oriented in opposite directions in the two regions of the pore of GlpF wild-type and GlpF ΔP177 separated by the NPA motif (Supplementary Fig. 13f). This finding is consistent with a previous report showing water molecule orientations in the GlpF pore[21].

MD simulations of GlpF wild-type and GlpF ΔP177 in POPC bilayers were conducted similarly for AQP3. The four chains in the tetramer had different initial conformations and velocities of atoms in the production run because of the energy minimisation and equilibration runs before it. The simulation length was sufficient for examining the structural stability and water distribution.

https://doi.org/10.1038/s41467-025-57728-3

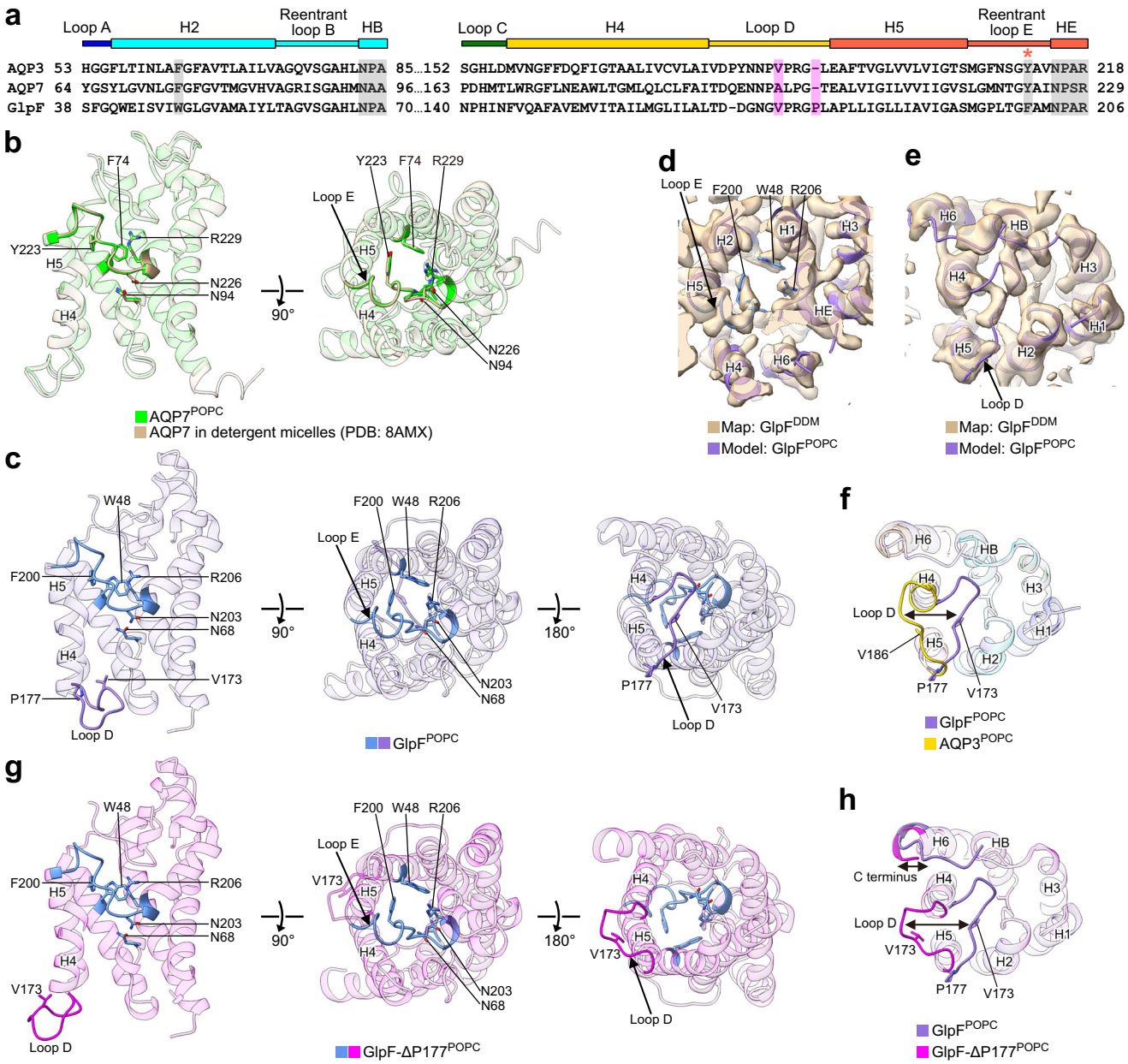

Fig. 5 | Structural comparison of AQP7 and GlpF with AQP3. a Aligned sequences of rat AQP3, human AQP7, and *E. coli* GlpF used in this study. Residues highlighted in gray are ar/R filter residues and NPA motifs. The site of residues corresponding to Tyr212 at reentrant loop E in AQP3 is indicated by an asterisk. Residues highlighted in pink correspond to GlpF Val173 and Pro177 at loop D, respectively. Sequence alignment was achieved by EMBL Clustal W web services, and manually modified. **b** Superimposition of overall structures of the monomers of AQP7 in POPC nanodiscs and reported AQP7 in the detergent micelles, which forms a dimer of tetramers analysed under D4 symmetry (PDB: 8AMX) from the side and extracellular views. The reentrant loop E, ar/R filter residues, and asparagines at the NPA motifs are highlighted with several residues shown as sticks. For clarity, loop B, loop C, and H6 are partially removed from the side views. **c** Overall structure of the monomer of $GlpF^{POPC}$ is shown as in (**b**). The intracellular view is also shown, and the intracellular loop D is highlighted with Val173 and Pro177 shown as sticks. **d**, **e** Superimposition of the model of $GlpF^{POPC}$ with the cryo-EM map of $GlpF^{DDM}$ from the extracellular (**d**) and intracellular (**e**) views. The ar/R filter residues are shown as sticks (**d**). **f** Comparison of the intracellular loop D of $GlpF^{POPC}$ and $AQP3^{POPC}$. The loop D is highlighted with several residues shown as sticks. The difference of loop D is indicated by a two-way arrow. **g** Overall structure of the monomer of GlpF-ΔP177^{POPC} is shown as in (**c**). **h** Comparison of $GlpF^{POPC}$ and GlpF-ΔP177^{POPC} from the intracellular view. The loop D and C-terminus are highlighted with several residues shown as sticks. The differences of loop D and C-terminus are indicated by two-way arrows.

We prepared GlpF wild-type and GlpF ΔP177 reconstituted POPC proteoliposomes, which had similar protein contents (Fig. 6i, Supplementary Fig. 13g, and Supplementary Table 1). Water permeability (Fig. 6j, Supplementary Fig. 13h, and Supplementary Table 1) and glycerol permeability (Fig. 6k, Supplementary Fig. 13i, and Supplementary Table 1) did not significantly differ between reconstituted GlpF wild-type and GlpF ΔP177.

Discussion

This study presents cryo-EM structures of aquaglyceroporins rat AQP3 and *E. coli* GlpF in DDM micelles and POPC nanodiscs, and human AQP7 in POPC nanodiscs, revealing distinct conformations among them (Supplementary Fig. 14). The narrowed pore structure of $AQP3^{POPC}$ through extracellular loop E with the insertion of Tyr212 into the pore is an AQP conformation not previously observed.

https://doi.org/10.1038/s41467-025-57728-3

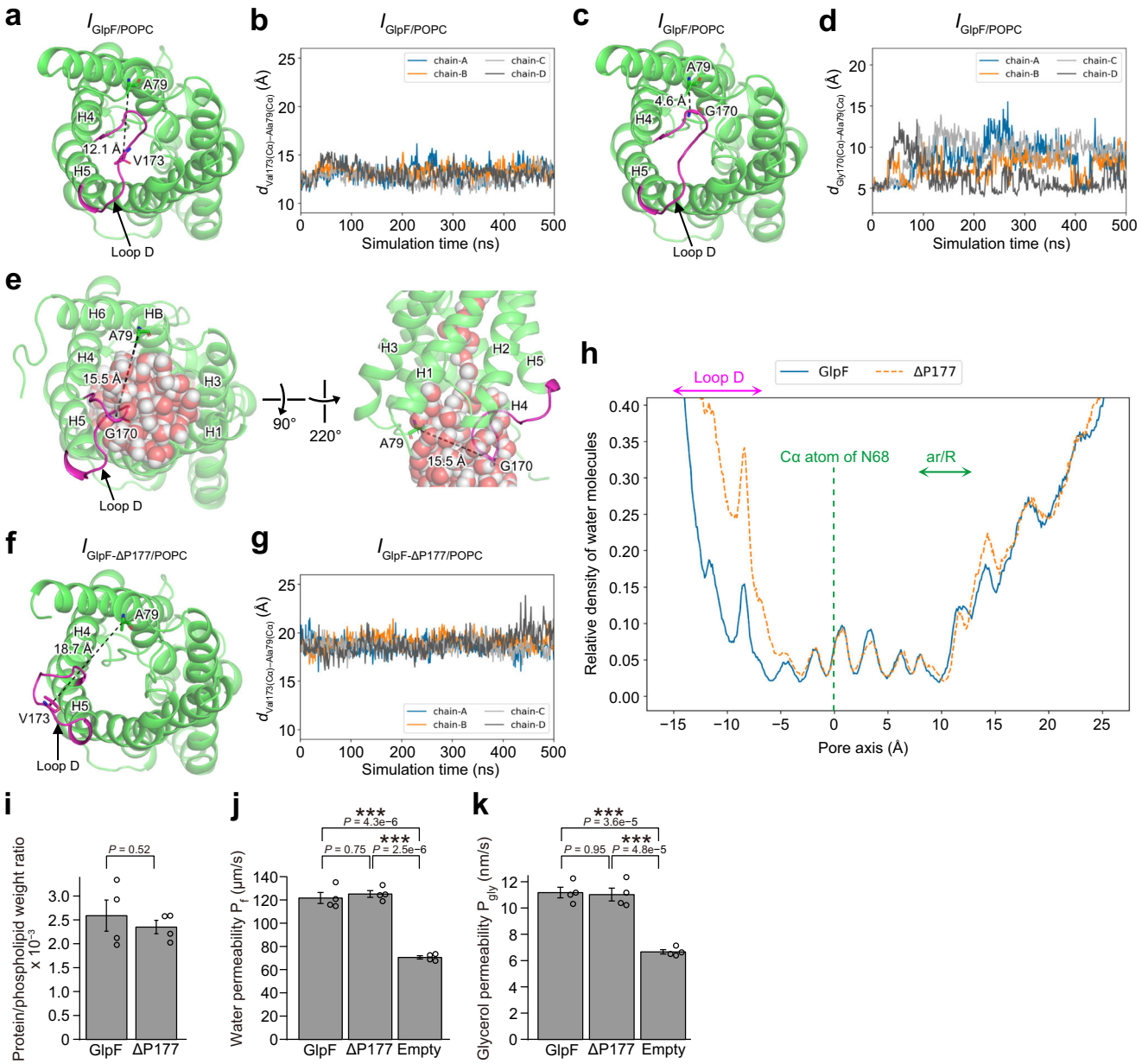

Fig. 6 | MD simulations and stopped-flow measurements of GlpF and its mutant. a–d Initial and monitored distance between Val173(Cα) and Ala79(Cα) (**a**, **b**) and between Gly170(Cα) and Ala79(Cα) (**c**, **d**) in MD simulations for $I_{GlpF/POPC}$. In the graphs of the monitored distance, the plots of the four chains of tetramers are shown (**b**, **d**). The loop D is represented by magenta (**a**, **c**). **e** Representative water distribution and the moved loop D in a snapshot for $I_{GlpF/POPC}$ during the MD simulation. The loop D and water molecules are represented by magenta and spheres, respectively. Initial (**f**) and monitored distance (**g**) between Val173(Cα) and Ala79(Cα) in MD simulations for $I_{GlpF-ΔP177/POPC}$. In the graphs of the monitored distance, the plots of the four chains of tetramers are shown (**g**). The loop D is represented by magenta. **h** Water distribution in pores during MD simulations for two systems. The pore axes are aligned with *z*-axes of the cryo-EM structures. The origin of the pore axis is set at the *z*-coordinate of Cα atom of Asn68. **i** The measured protein/phospholipid weight ratio of GlpF and GlpF ΔP177 proteoliposomes. Averaged values ± SEM and individual data points are plotted ($n = 4$ independently reconstituted liposome samples from the same purified proteins). Data are statistically analysed using Student's two-tailed unpaired *t* test. *P* value is indicated. **j** Stopped-flow measurements under NaCl hyperosmotic conditions for GlpF and GlpF ΔP177 proteoliposomes and empty liposomes. Averaged water permeability P_f values ± SEM and individual data points are plotted ($n = 4$ independently reconstituted liposome samples from the same purified proteins). Data are statistically analysed using multiple comparison Tukey test. *P* values are indicated. ***$P < 0.001$. **k** Stopped-flow measurements under glycerol gradient conditions for GlpF and GlpF ΔP177 proteoliposomes and empty liposomes. Averaged glycerol permeability P_{gly} values ± SEM and individual data points are plotted ($n = 4$ independently reconstituted liposome samples from the same purified proteins). Data are statistically analysed using multiple comparison Tukey test. *P* values are indicated. ***$P < 0.001$. Source data are provided as a Source Data file.

We purified DDM-solubilised AQP3 from insect cells. The cryo-EM structure of $AQP3^{DDM}$ showed that the ar/R filter containing Tyr212 forms a pore with a 2.8-Å diameter (Tyr212-out conformation; Fig. 1e). The stability of the reentrant loop E containing Tyr212 represented by the B-factor of cryo-EM structure of $AQP3^{DDM}$ was inconsistent with fluctuations observed in the Tyr212-out conformations by MD simulations (Supplementary Fig. 8f, g). We observed an unassigned cryo-EM density map at the pore of $AQP3^{DDM}$ (Fig. 1h); the unassigned density might stabilise the Tyr212-out conformation and inhibit the Tyr212-in conformation in the cryo-EM structure of $AQP3^{DDM}$. The cryo-EM structure of AQP3-Y212T^{DDM} exhibits an apparent DDM density at the pore inserted from the intracellular side (Fig. 3i), suggesting that

the unassigned density observed in the pore of AQP3^{DDM} might also correspond to DDM. Due to the unclear map shape, however, it was difficult to assign DDM or lipids in the cryo-EM map of AQP3^{DDM} pore.

AQP3 was reconstituted into POPC nanodiscs by mixing DDM-solubilised AQP3 with MSP proteins and POPC, followed by the application of Bio-Beads to remove the DDM. The cryo-EM structure of AQP3^{POPC} showed that Tyr212 inserts into the pore (Tyr212-in conformation; Fig. 1f). The Tyr212-in conformation is the only conformation reconstructed during the cryo-EM data processing (Supplementary Fig. 2d), although we cannot exclude the possibility that the protein particles that form the Tyr212-out conformation are mixed in the micrographs. The three-dimensional (3D) classification also showed that smaller and larger size of MSP nanodiscs are mixed, but both exhibited the Tyr212-in conformation (Supplementary Fig. 2d), suggesting that the interaction between AQP3 and MSP is not important for the Tyr212-in conformation. This is further supported by cryo-EM analysis of AQP3^{DMPC} because one monomer (Monomer B; Supplementary Fig. 7a, b) that does not seem to interact with the MSP disc forms the Tyr212-in conformation. Structures of AQP3^{POPC} and AQP3^{DMPC} suggest that the Tyr212-in conformation does not depend on the length of the acyl chain in PC lipids.

Cryo-EM structures of AQP3 mutants in POPC nanodiscs suggest that aromatic residue Tyr212 or Y212F must stably insert into the AQP3 pore (Fig. 3a). We speculate that the positive electrostatic field at the NPA motifs, generated by the helical dipole moment of the two short HB and HE helices, attracts the pi-electrons of the aromatic residue to stabilise the AQP3 structure. The aromatic residue itself is not sufficient to insert into the pore in POPC nanodiscs, as the pore narrowed by reentrant loop E is not observed in AQP7 and GlpF, although they share aromatic residues Tyr223 and Phe200 at the position corresponding to Tyr212 in AQP3 (Fig. 5b, c). AQP3 contains unique sequences that are not present in AQP7 and GlpF, but may be critical for forming the Tyr212-in conformation.

The Tyr212-in conformation of AQP3^{POPC} is a pore-occluded state as calculated by the pore detection programme MOLEonline (Supplementary Fig. 4b) and as supported by MD simulations of the water distribution in the AQP3 Tyr212-in conformation within the POPC bilayer system (Fig. 2g). AQP3 is a known aquaglyceroporin, and we confirmed that AQP3 reconstituted in POPC liposomes exhibits both water and glycerol permeability (Fig. 4). Therefore, we speculate that, upon the permeation of water and glycerol, the AQP3 Tyr212-in conformation undergoes conformational rearrangement in the plug loop, transitioning to a water- or glycerol-permeable state, possibly resembling the Tyr212-out conformation.

The water and glycerol permeability of AQP3 Y212F in POPC liposomes is similar to that of AQP3 wild-type (Fig. 4). This is consistent with the cryo-EM structure of AQP3-Y212F^{POPC} in which Y212F is inserted into the pore like AQP3 wild-type (Fig. 3a). The water and glycerol permeability of AQP3 Y212T is slightly faster than that of AQP3 wild-type and AQP3 Y212F (Fig. 4). This may be consistent with the cryo-EM structure of AQP3-Y212T^{POPC}, in which Y212T is not inserted into the pore (Fig. 3b), and a wider pore is detected compared with AQP3^{POPC} and AQP3-Y212T^{POPC} (Supplementary Fig. 4b). The loop E containing Y212T might be sufficiently flexible to allow water and glycerol to pass through in the POPC environment.

We present cryo-EM structural evidence for GlpF with pore capping by intracellular loop D both in DDM micelles and POPC nanodiscs (Fig. 5c, e). Loop D does not cap the pore in the X-ray crystal structure of GlpF, suggesting that crystal packing may account for the differences between the X-ray crystal and cryo-EM structures of GlpF. Intracellular loop D caps the pore in the cryo-EM structure of GlpF^{POPC}, but the loop D is suggested to be flexible by its B-factor (Supplementary Fig. 13e). MD simulations of GlpF in POPC bilayer support that the intracellular loop D is flexible and that water molecules could pass through near the loop D (Fig. 6a–e, h and Supplementary Fig. 13d). We found that the loop D conformation exhibits an open pore in GlpF-ΔP177^{POPC} (Fig. 5g). MD simulations and stopped-flow measurements using GlpF wild-type and ΔP177 (Fig. 6) suggest that the narrowed pore conformation by intracellular loop D is not largely related to the GlpF permeability. This may be similar to the case of OsNIP2;1 loop D, in which MD simulations showed a rapid opening of the loop D and its physiological significance remains to be elucidated[36,37]. In contrast, for SoPIP2;1, the low pH keeps the SoPIP2;1 loop D closed, and phosphorylation is proposed to modulate loop D gating[38,39].

In addition to the narrowed pore structures of AQPs by loop D capping and AQP3 by pore-inserted loop E, other narrowed AQP structures are reported. The X-ray crystal structure of yeast Aqy1 shows its intracellular N-terminus blocking the pore[40]. The X-ray crystal structure of AQP10 shows a pH-dependent closed state by intracellular loop B[29]. The X-ray crystal structure of the freshwater fish climbing perch AQP shows that extracellular loop C narrows the pore[41]. The electron crystal structure of AQP0 shows that junctions are formed via extracellular loops with a closed conformation[42,43]. Thus, AQPs appear to have diverse narrowed pore conformations.

In conclusion, we identified distinct conformations of aquaglyceroporins AQP3, AQP7, and GlpF, and revealed AQP3-specific narrowed pore conformation by the insertion of Tyr212 in an extracellular loop. AQP3 is localised in skin keratinocytes, contributing to physiological and pathological skin conditions[44,45]. AQP3 is also involved in cancer progression[46]. Our newly uncovered structural information may contribute to the development of chemicals and drugs targeting AQP3.

Methods

DNA constructs

Complementary DNAs of rat AQP3 and human AQP7 proteins (Uniprot: P47862 and O14520, respectively) were cloned from cDNA libraries, while that of *E. coli* (strain K12) GlpF protein (Uniprot: P0AER0) was commercially synthesised. The full-length genes were subcloned into the pFastBac vector (Invitrogen) using the Gibson assembly system (New England Biolabs). For AQP3 and GlpF, additional residues, including an octa-His tag, a thrombin digestion site, and a linker sequence, were attached at the N-terminus. For AQP7, additional residues, including an octa-His tag, enhanced green fluorescent protein (A207K), a tobacco etch virus protease digestion site, and a linker sequence, were attached at the N-terminus. Site-directed mutagenesis was achieved by overlap extension polymerase chain reaction.

Expression and purification of MSP proteins

Plasmids for MSP1D1 and MSP1E3D1 expression were purchased from Addgene (Addgene plasmid nos. 20,061 and 20,066)[47,48]. The plasmids were transformed into BL21-Gold(DE3) (Agilent), which was cultured at 37 °C. Expression of MSP proteins was induced by isopropyl β-D-thiogalactopyranoside. The harvested cells were suspended in buffer containing 40 mM Tris (pH 8.0), 300 mM NaCl, 1% (v/v) Triton X, and 1 mM phenylmethylsulfonyl fluoride, and then disrupted by sonication. The sonicated cell suspension was centrifuged at 22,095 × *g* for 25 min. The collected supernatant was bound to nickel-nitrilotriacetic acid-agarose resin (Ni-NTA, Qiagen) under 1 mM L-His for 5 h. The resin was washed with 50 mM sodium cholate and 20 mM imidazole and then eluted with buffer containing 40 mM Tris (pH 8.0), 300 mM NaCl, and 450 mM imidazole. The eluate was dialysed in buffer containing 20 mM Tris (pH 8.0) and 150 mM NaCl. Tobacco etch virus protease was incubated, and then Ni-NTA was mixed to remove the tag. The pass fractions were collected and dialysed in buffer containing 20 mM Tris (pH 8.0) and 150 mM NaCl.

Expression, purification, and nanodisc reconstitution of AQPs

All constructs were expressed in Sf9 (Novagen, 71104) or Sf+ (Protein Sciences Corporation) insect cells using the Bac-to-Bac Baculovirus

Expression System (Invitrogen). Cells were cultured in suspension at 27 °C, harvested after 48 h infection, and stored at −80 °C.

For AQP7, cells were suspended in a phosphate-buffered saline buffer supplemented with 2 mM EDTA and 1 mM phenylmethylsulfonyl fluoride, and then disrupted by sonication. The sonicated cell suspension was centrifuged at 960 × *g* for 10 min, and the supernatant was centrifuged at 100,000 × *g* for 45 min. The collected crude membranes were solubilised for 1 h at 4 °C in buffer containing 20 mM Tris (pH 8.0), 300 mM NaCl, and 1% (w/v) DDM. After centrifugation at 100,000 × *g* for 45 min, the detergent concentration of the supernatant was decreased to 0.2% DDM by dilution and bound to Ni-NTA under 10 mM imidazole overnight. The resin was washed with 50 mM imidazole and then eluted with 300 mM imidazole in buffer containing 20 mM Tris (pH 8.0), 300 mM NaCl, and 0.05% DDM. The eluate was concentrated and loaded onto a Superose 6 Increase 10/300 GL column (Cytiva) equilibrated with buffer containing 20 mM Tris (pH 8.0), 150 mM NaCl, and 0.05% DDM. Peak fractions were pooled as AQP7 in DDM micelles. MSP1E3D1 was used to reconstitute DDM-solubilised AQP7 into nanodiscs. POPC lipids in chloroform were dried using nitrogen gas and rehydrated with 2% DDM. The AQP-monomer:MSP:POPC molar ratio for AQP7 was 1:0.5:30. Mixed samples were incubated with Bio-Beads SM-2 resin (Bio-Rad) overnight at 4 °C with constant rotation. The mixture, except for the Bio-Beads, was mixed with Ni-NTA to remove empty nanodiscs. The eluate was concentrated and loaded onto a Superose 6 Increase 10/300 GL column in buffer containing 20 mM Tris (pH 8.0) and 150 mM NaCl. Peak fractions were pooled as AQP7 in POPC nanodiscs.

For AQP3, GlpF, and their mutants, cells were suspended in buffer containing 20 mM Tris (pH 7.5) and 150 mM NaCl, and then disrupted by sonication. The sonicated cell suspension was centrifuged at 960 × *g* for 10 min, and the supernatant was centrifuged at 100,000 × *g* for 30 min. The collected crude membranes were solubilised in buffer containing 20 mM Tris (pH 7.5), 150 mM NaCl, 5% (v/v) glycerol, and 1% DDM for 1 h at 4 °C. After centrifugation at 100,000 × *g* for 30 min, the DDM concentration of the supernatant was decreased to 0.4% by dilution and bound to Ni-NTA under 1 mM L-His for approximately 3 h. The resin was washed with 5 mM L-His and then eluted with 300 mM L-His in buffer containing 20 mM Tris (pH 7.5), 150 mM NaCl, 5% glycerol, and 0.03% DDM. The eluate was concentrated and loaded onto a Superose 6 Increase 10/300 GL column in buffer containing 20 mM Tris (pH 7.5), 150 mM NaCl, and 0.03% DDM. Peak fractions were pooled as AQP3, GlpF, or their mutants in DDM micelles, and reconstituted into nanodiscs using MSP1D1. The AQP-monomer:MSP:POPC molar ratios were as follows: 1:5:200 for $AQP3^{POPC}$, $AQP3\text{-}Y212F^{POPC}$, and $AQP3^{DMPC}$; and 1:5:50 for $AQP3\text{-}Y212T^{POPC}$, $GlpF^{POPC}$, and $GlpF\text{-}\Delta P177^{POPC}$. Mixed samples were incubated with Bio-Beads SM-2 resin overnight at 4 °C with constant rotation, except for $AQP3^{DMPC}$ at room temperature. The mixture, except for the Bio-Beads, was concentrated and loaded onto a Superose 6 Increase 10/300 GL column in buffer containing 20 mM Tris (pH 7.5) and 150 mM NaCl. Two peaks appeared to correspond to AQPs in nanodiscs and empty nanodiscs. The first peak fractions containing AQPs in nanodiscs were mixed and bound to Ni-NTA to further remove the contaminated empty nanodiscs. The eluate was concentrated and loaded onto a Superose 6 Increase 10/300 GL column in buffer containing 20 mM Tris (pH 7.5) and 150 mM NaCl. Peak fractions were pooled as AQP3, GlpF, or their mutants in nanodiscs.

The LabAssay Phospholipid Kit (FUJIFILM Wako) and SpectraMax i3x microplate reader (Molecular Devices) were used to measure the phospholipid concentrations in the purified proteins of $AQP3^{DDM}$ and $AQP3^{POPC}$ diluted to an absorbance at 280 nm of 3. AQP3 monomer concentration in the diluted purified $AQP3^{DDM}$ was calculated to be 2.2 mg/mL from the absorbance and molar extinction coefficient. The purified $AQP3^{POPC}$ contains AQP3 and MSP1D1 proteins. The weight ration of AQP3:MSP1D1 was estimated to be 2:1 by sodium dodecyl sulphate-polyacrylamide gel electrophoresis analysis (Supplementary Fig. 1b). Therefore, AQP3 concentration in the diluted purified $AQP3^{POPC}$ was estimated to be 1.7 mg/mL from the absorbance and molar extinction coefficients of AQP3 and MSP1D1. The detected phospholipid concentrations were represented as the normalised phospholipid concentrations for AQP3 concentration of 1 mg/mL.

Cryo-EM data acquisition

The purified AQPs were concentrated at the appropriate concentrations as follows: 0.7–2.9 mg/mL for AQPs in lipid nanodiscs; 19 mg/mL for $AQP3^{DDM}$; and 5.0 mg/mL for $AQP3\text{-}Y212T^{DDM}$ and $GlpF^{DDM}$. The concentrated proteins were loaded onto glow-discharged Quantifoil holey carbon grids (R1.2/1.3, Au, 300 mesh), which were blotted for approximately 4.0 s at 4 °C and plunge-frozen in liquid ethane using a Vitrobot Mark IV (Thermo Fisher Scientific). Data collection was performed on a JEM-Z320FHC electron microscope (JEOL, Japan) cooled by liquid nitrogen at 300 kV, equipped with a cold field emission gun and an in-column energy filter using a zero-loss slit width of 20 eV. All images were recorded on a K2 Summit direct electron detector camera (Gatan) operated in electron counting mode. SerialEM[49] was used for automatic data acquisition. The dose rate was limited to 8.0 e^-/pixel/s, and the exposure time was 8.0 s and fractionated into 40 frames without a pre-dose delay. The refined pixel size and the accumulated dose for each sample of AQPs are summarised in Supplementary Table 2.

Cryo-EM data processing

All image processing was performed using RELION[50,51] and cryoSPARC[52]. The stacked frame movies were subjected to motion correction with MotionCor2[53] in RELION. Contrast transfer function (CTF) estimation was performed with cryoSPARC patch CTF algorithm. Micrographs with an estimated resolution worse than 4 or 5 Å were removed. Initial particles were picked from the yielded micrographs by the blob picker or the template picker using fine two-dimensional (2D) class averages in cryoSPARC. The initial particles were subjected to multiple rounds of 2D classification and selected for heterogeneous refinement in cryoSPARC. After heterogeneous refinement using multiple reference maps generated from ab-initio reconstruction or 3D refinement, the classified particles were subjected to homogeneous refinement and non-uniform (NU) refinement[54] in cryoSPARC. These refined particles were then imported to RELION using the PyEM algorithm [https://doi.org/10.5281/zenodo.3576630], followed by 3D refinement, Bayesian polishing[55], and 3D classification without alignment in RELION. The classified particles were imported back to cryoSPARC for 2D classification and finally subjected to NU refinement and global CTF refinement. Map resolutions under the refined pixel sizes were estimated according to the gold-standard Fourier shell correlation using the 0.143 criterion[56] in cryoSPARC (Supplementary Fig. 3). Local resolution was estimated in cryoSPARC.

For $AQP3^{DDM}$ (Supplementary Fig. 2a, c, e), 3251 movies were collected, yielding 2470 micrographs, 1,948,354 initial particles, and 385,812 selected particles for heterogeneous refinement under C1 symmetry. The selected 172,527 particles after the heterogeneous refinement were processed by Bayesian polishing and 3D classification without alignment in RELION. The selected 161,557 particles were imported back to cryoSPARC for 2D classification and NU refinement under C4 symmetry with global CTF refinement. Finally, a 3.12 Å resolution map was obtained from 153,591 particles.

For $AQP3^{POPC}$ (Supplementary Fig. 2b, d, f), 1557 and 6012 movies from two datasets were collected, yielding 1362 and 5174 micrographs, 1,216,419 and 4,627,389 initial particles, and 198,592 and 788,271 selected particles for heterogeneous refinement under C1 symmetry. The 351,377 selected particles after the heterogeneous refinement were processed by Bayesian polishing and 3D classification without alignment in RELION. The selected 279,337 particles were

imported back to cryoSPARC for 2D classification and NU refinement under C4 symmetry with global CTF refinement. Finally, a 2.94 Å resolution map was obtained from 271,900 particles.

For AQP3^{DMPC}, 6021 movies were collected, yielding 5454 micrographs, 4,890,341 initial particles, and 1,081,920 selected particles for heterogeneous refinement under C1 symmetry. The selected 500,069 particles after the heterogeneous refinement were processed by Bayesian polishing and 3D classification without alignment in RELION. The selected 236,611 particles were imported back to cryoSPARC for 2D classification and NU refinement under C1 symmetry with global CTF refinement. Finally, a 3.03 Å resolution map was obtained from 228,009 particles.

For AQP3-Y212F^{POPC}, 6885 movies were collected, yielding 6320 micrographs, 4,658,285 initial particles, and 810,927 selected particles for heterogeneous refinement under C1 symmetry. The selected 240,685 particles after the heterogeneous refinement were processed by Bayesian polishing and 3D classification without alignment in RELION. The selected 145,026 particles were imported back to cryoSPARC for 2D classification and NU refinement under C4 symmetry with global CTF refinement. Finally, a 2.90 Å resolution map was obtained from 135,650 particles.

For AQP3-Y212T^{POPC}, 7713 movies were collected, yielding 6781 micrographs, 6,873,017 initial particles, and 1,854,449 selected particles for heterogeneous refinement under C1 symmetry. The selected 756,357 particles after the heterogeneous refinement were processed by Bayesian polishing and 3D classification without alignment in RELION. The selected 308,080 particles were imported back to cryoSPARC for 2D classification and NU refinement under C4 symmetry with global CTF refinement. Finally, a 2.67 Å resolution map was obtained from 295,521 particles.

For AQP3-Y212T^{DDM}, 4887 movies were collected, yielding 4250 micrographs, 1,789,455 initial particles, and 334,358 selected particles for heterogeneous refinement under C4 symmetry. The selected 127,686 particles after the heterogeneous refinement were processed by Bayesian polishing and 3D classification without alignment in RELION. The selected 60,523 particles were imported back to cryoSPARC for 2D classification and NU refinement under C4 symmetry with global CTF refinement. Finally, a 3.39 Å resolution map was obtained from 54,899 particles.

For AQP7^{POPC}, 3636 movies were collected, yielding 3010 micrographs, 3,638,849 initial particles, and 148,023 selected particles from iterative heterogeneous refinement under C4 symmetry. The selected particles were processed by Bayesian polishing in RELION. The particles were imported back to cryoSPARC for NU refinement under C4 symmetry with global CTF refinement. Finally, a 2.49 Å resolution map was obtained.

For GlpF^{DDM}, 4012 and 6264 movies from two datasets were collected, yielding 3762 and 5676 micrographs, 993,334 and 1,380,923 initial particles, and 162,007 and 118,824 selected particles for heterogeneous refinement under C1 symmetry. The selected 139,789 particles after the heterogeneous refinement were processed by Bayesian polishing and 3D classification without alignment in RELION. The selected 112,714 particles were imported back to cryoSPARC for 2D classification and NU refinement under C4 symmetry with global CTF refinement. Finally, a 3.74 Å resolution map was obtained from 110,202 particles.

For GlpF^{POPC} (Supplementary Fig. 12a), 4824 movies were collected, yielding 4318 micrographs, 4,067,871 initial particles, and 1,171,447 selected particles for heterogeneous refinement under C1 symmetry. The selected 520,152 particles after the heterogeneous refinement were processed by Bayesian polishing and 3D classification without alignment in RELION. The selected 268,667 particles were imported back to cryoSPARC for 2D classification and NU refinement under C4 symmetry with global CTF refinement. Finally, a 2.43 Å resolution map was obtained from 252,983 particles.

For GlpF-ΔP177^{POPC} (Supplementary Fig. 12c), 8100 movies were collected, yielding 6934 micrographs, 8,748,925 initial particles, and 2,231,512 selected particles for heterogeneous refinement under C1 symmetry. The selected 1,062,495 particles after the heterogeneous refinement were processed by Bayesian polishing and 3D classification without alignment in RELION. The selected 475,168 particles were imported back to cryoSPARC for 2D classification and NU refinement under C4 symmetry with global CTF refinement. Finally, a 2.26 Å resolution map was obtained from 462,907 particles.

Model building and refinement

AlphaFold structures[57,58] were used as starting models for AQP3^{DDM}, AQP7^{POPC}, and GlpF^{POPC}. The obtained cryo-EM maps were processed in the *Servalcat* pipeline[59] to trim the maps with the refined pixel sizes. Model refinement using *Coot*[60] and real-space refinement in *PHENIX*[61] were iterated. The refined models were C4 symmetry imposed in the *Servalcat* pipeline except for AQP3^{DMPC}. The geometry was evaluated using MolProbity[62]. The final refinement statistics are summarised in Supplementary Table 2. The molecular graphics figures were prepared using UCSF ChimeraX[63]. Pore radius of AQPs was calculated using MOLEonline server v.2.5 pore mode[64].

Reconstitution of AQPs into proteoliposomes

POPC lipids in chloroform were dried using nitrogen gas, freeze-dried under vacuum, and rehydrated with buffer containing 20 mM Tris (pH 7.5) and 150 mM NaCl, followed by sonication. The POPC solution was diluted to 1 mg/mL with 0.1% DDM. The pooled DDM-solubilised AQPs were diluted to 0.1 mg/mL. The AQP-monomer:POPC weight ratios were ~1:800 for mixing. Bio-Beads SM-2 resin was added and incubated overnight at 4 °C with constant rotation. The mixture, except for the Bio-Beads, was subjected to ultracentrifuge at 100,000 × *g* for 20 min. The collected pellet was suspended and sonicated in buffer containing 20 mM Tris (pH 7.5) and 150 mM NaCl. The empty liposomes were made without AQPs. To measure the concentrations of proteins and phospholipids in the proteoliposomes and empty liposomes, the SYPRO Ruby stain (Thermo Fisher Scientific) of sodium dodecyl sulphate-polyacrylamide gel electrophoresis analysis gels and the LabAssay Phospholipid Kit were used, respectively. The SYPRO Ruby fluorescence was detected using a light-emitting diode transilluminator and analysed using Fiji software. The fluorescence intensity of the protein marker (XL-Ladder; Apro Science) was used to estimate protein concentrations.

Stopped-flow analysis

The 20 µL reconstituted samples diluted up to 1750 µL with buffer containing 20 mM Tris (pH 7.5) and 150 mM NaCl were used for measurements carried out on a SX20 stopped-flow spectrometer (Applied Photophysics). Measurements under hyperosmotic conditions were obtained by mixing diluted samples and the same volume of buffer containing 20 mM Tris (pH 7.5) and 250 mM NaCl, resulting in an outer buffer containing 20 mM Tris (pH 7.5) and 200 mM NaCl, leading to a 50-mM inwardly directed NaCl gradient. Another measurement was obtained by mixing diluted samples and the same volume of buffer containing 20 mM Tris (pH 7.5), 150 mM NaCl, and 200 mM glycerol, resulting in an outer buffer containing 20 mM Tris (pH 7.5), 150 mM NaCl, and 100 mM glycerol, leading to a 100-mM inwardly directed glycerol gradient. The kinetics of vesicle shrinkage or swelling were measured by recording the change in intensity of 90° scattered light at a wavelength of 450 nm at 20 °C over time.

The change in signal intensity under NaCl hyperosmotic conditions was calculated by subtracting the averaged intensity from 0.10 to 0.14 s and normalised by the maximum intensity from 0.10 to 1.5 s. The time course of the intensity change under NaCl hyperosmotic conditions was plotted from 0.10 to 1.5 s and fitted to a single-exponential curve to determine the rate constant k using IGOR Pro (WaveMetrics).

The sizes of proteoliposomes and empty liposomes were verified by a particle analyser (ELSZ, Otsuka Electronics) at 20 °C. The water permeability coefficient (P_f) under hyperosmotic conditions was calculated according to the following equation as previously described[29]: $P_f = (k \times V_0)/(\Delta C \times V_w \times A)$, where V_0 is the volume of the liposome sample, A is the surface area of the liposome sample, ΔC is the osmotic gradient, and V_w is the molar volume of water.

The change in signal intensity under glycerol gradient conditions was calculated by subtracting the minimum intensity from 0.10 to 10 s and normalised by the maximum intensity from 0.10 to 10 s. The time course of the intensity change under glycerol gradient conditions was plotted from 0.10 to 10 s. The glycerol permeability (P_{gly}) was calculated from the following equation as previously described[29,65]: $P_{gly} = 1/((S/V) \times \tau)$, where S/V is the surface-to-volume ratio and τ is the exponential time constant fitted to the swelling phase of light scattering time course.

Statistics and reproducibility

All data are presented as means along with the standard error of the mean (SEM). The phospholipid concentrations in the purified proteins were measured in triplicate from the same purified proteins. Measurements using proteoliposomes and empty liposomes were performed in triplicate or tetraplicate from independently reconstituted liposome samples. The statistical analyses were performed using Student's two-tailed unpaired *t* test in Excel (Microsoft) and multiple comparison Tukey test in IGOR Pro. A value of $P < 0.05$ was considered significant. The purification of each AQP protein by the detergent was examined at least two times, and it was reliably reproduced.

MD simulations

For MD simulations of AQP3, the initial structures were modelled using the cryo-EM structures exhibiting the Tyr212-out conformation ($AQP3^{DDM}$) and the Tyr212-in conformation ($AQP3^{POPC}$). In the modelling, we used the residues from Tyr19 to Glu270 of the AQP3 structures. The AQP3 structures were modelled as a tetramer generating symmetry copies with ChimeraX[63]. The protonation states were determined based on $AQP3^{POPC}$ structure, using PROPKA[66] available in Maestro (Schrödinger, LLC, USA) and assuming an aqueous environment at pH 7.5. Both the Tyr212-out and Tyr212-in conformations of AQP3 were buried in DDM micelles and in a POPC lipid bilayer using Micelle Builder and Bilayer Builder, respectively, of the CHARMM-GUI web server[67–75]. The number of DDM molecules was adjusted to 280 per AQP3 tetramer to prevent gaps and holes in the micelles. The position of the membrane for AQP3 was determined from that for AQP7 (PDB: 6QZI)[25] available in OPM database[76]. Thus, four systems for MD simulations were generated and referred to as $I_{Tyr212\text{-}out/DDM}$, $I_{Tyr212\text{-}out/POPC}$, $I_{Tyr212\text{-}in/DDM}$, and $I_{Tyr212\text{-}in/POPC}$ (Supplementary Fig. 8a–d). The generated solution systems were neutralised adding Na^+ and Cl^- ions, where the concentration of ions was set at 0.15 mol/L. The number of atoms in the generated systems was 260,379 for $I_{Tyr212\text{-}out/DDM}$, 120,262 for $I_{Tyr212\text{-}out/POPC}$, 259,012 for $I_{Tyr212\text{-}in/DDM}$, and 121,615 for $I_{Tyr212\text{-}in/POPC}$.

The MD simulations for the four systems were conducted using GROMACS 2022[77]. The employed force field for protein was CHARMM36m[78], and that for DDM and POPC was CHARMM36[79–83]. The setup of the force fields is the default one of Micelle Builder and Bilayer Builder of CHARMM-GUI[67–75]. In particular, the force fields of protein and POPC are often used for MD simulations in membrane–protein systems. As the water model, TIP3P[84] was employed. The bond lengths involving hydrogens were constrained using LINCS[85]. The electrostatic interactions were calculated using the Particle Mesh Ewald method[86]. The van der Waals interactions were smoothly truncated over 1.0–1.2 nm. Before the MD simulation production runs, the energy minimisation by the steepest descent method and six equilibration runs, referred to as EQ1–EQ6 hereafter, were conducted sequentially according to the default setup of Micelle Builder and Bilayer Builder of CHARMM-GUI[67–75]. EQ1 and EQ2 were conducted in the NVT ensemble at 300 K, and EQ3–EQ6 were conducted in the NPT ensemble at 300 K and 1 atm. The thermostat in EQ1–EQ6 was the weak-coupling scheme of Berendsen[87], and the barostat in EQ3–EQ6 was the isotropic Berendsen algorism[87] for $I_{Tyr212\text{-}out/DDM}$ and $I_{Tyr212\text{-}in/DDM}$ and semi-isotropic Berendsen[87] for $I_{Tyr212\text{-}out/POPC}$ and $I_{Tyr212\text{-}in/POPC}$. The timestep and simulation length were set to 0.001 and 125 ps, respectively, in EQ1–EQ3 and to 0.002 and 500 ps, respectively, in EQ4–EQ6. In the energy minimisation and EQ1–EQ6, structural restraints with reference to the initial structures were applied, the force constants of which were reduced in a stepwise manner from EQ1 to EQ6. The ranges of force constants from EQ1 to EQ6 were 4000–50 kJ/mol/nm^2 for backbone atoms of protein, 2000–0 kJ/mol/nm^2 for sidechain non-hydrogen atoms, 1000–0 kJ/mol/nm^2 for positional restraints of DDM and POPC molecules, and 1000–0 kJ/mol/rad^2 for dihedral restraints of DDM and POPC molecules. The force constants in the energy minimisation were the same as those in EQ1. Positional restraints were imposed on carbon atoms connecting the tail and head group of DDM and on the *z*-coordinate of the phosphorus atoms of POPC. Dihedral restraints were imposed on 12 bonds involving carbon and oxygen atoms forming the two sugar rings in the head group of DDM and on the double bond between carbon atoms in the oleic acids of POPC.

After the equilibration runs, a 500 ns production run (timestep = 0.002 ps) was conducted for each of the four systems. The NPT ensemble at 300 K and 1 atm was employed in all production runs. The thermostat was the Nosé–Hoover method[88,89], and the barostat was the isotropic Parrinello–Rahman method[90,91] for $I_{Tyr212\text{-}out/DDM}$ and $I_{Tyr212\text{-}in/DDM}$ and semi-isotropic Parrinello–Rahman[90,91] for $I_{Tyr212\text{-}out/POPC}$ and $I_{Tyr212\text{-}in/POPC}$. Snapshots taken every 100 ps were used for analysis.

In a similar manner, to conduct MD simulations of GlpF, the initial structures were modelled using the cryo-EM structures exhibiting pore capped by loop D ($GlpF^{POPC}$) and pore opening ($GlpF\text{-}\Delta P177^{POPC}$). In the modelling, we used the residues from Ser5 to Cys261 of the $GlpF^{POPC}$ structure and the residues from Ser5 to Gly256 of the $GlpF\text{-}\Delta P177^{POPC}$ structure. The GlpF and GlpF-ΔP177 structures were modelled as a tetramer using ChimeraX[63]. The protonation states were determined based on the $GlpF^{POPC}$ structure, using PROPKA[66] of Maestro. Both the modelled open and capped pore structures of GlpF were buried in a POPC lipid bilayer using Bilayer Builder of CAHRMM-GUI[67–75]. The position of the membrane for GlpF was determined from that for GlpF (PDB: 1LDF)[21] available in OPM database[76]. The two systems for MD simulations are referred to as $I_{GlpF/POPC}$ and $I_{GlpF\text{-}\Delta P177/POPC}$ (Supplementary Fig. 13a, b). The generated systems were neutralised by adding Na^+ and Cl^- ions, where the concentration of ions was set at 0.15 mol/L. The number of atoms in the generated systems is 128,094 for $I_{GlpF/POPC}$ and 122,487 for $I_{GlpF\text{-}\Delta P177/POPC}$. According to the same setup used for $I_{Tyr212\text{-}out/POPC}$ and $I_{Tyr212\text{-}in/POPC}$ of AQP3, the energy minimisation, equilibration runs, and production runs were conducted.

To investigate distributions of water molecules within the AQP3 pores, the pore regions were defined as cylinders with a radius of 8 Å, the central axes of which pass through the intermediate points between Cα atoms of Asn83 and Val195. Aligning AQP3 structures of all MD snapshots with the initial structures, the central axes of the pores were set in parallel to the *z*-axes. Dividing the defined pore region into small cylinders every 0.1 Å along the central axis, the number of oxygen atoms of water molecules within each small cylinder was counted for all snapshots, which provided the simulated distributions of water molecules within the pores for $I_{Tyr212\text{-}out/DDM}$, $I_{Tyr212\text{-}out/POPC}$, $I_{Tyr212\text{-}in/DDM}$, and $I_{Tyr212\text{-}in/POPC}$. In the same manner, the water distribution for GlpF was calculated. The central axis of the defined pore region for GlpF passes through the intermediate point between Cα atoms of Asn68 and Val52. The water molecules that passed through the pores were also counted for all MD trajectories. The number of oxygen atoms

in the water molecules that passed was counted, which was the sum of both the passage in the extracellular direction and that in the intracellular direction. The water orientation in the pores was also calculated. The order parameter of water orientation was defined as the averaged cosθ, where θ of a water molecule is the angle between its dipole moment and the pore axis. The MD trajectories were analysed using Ambertools22[92]. The structural snapshots and movies of MD simulations were visualised by Pymol (Schrödinger, LLC, USA) and VMD[93], respectively.

Details of the system setup for AQP3 and GlpF MD simulations are provided in Supplementary Tables 3 and 4.

Reporting summary

Further information on research design is available in the Nature Portfolio Reporting Summary linked to this article.

Data availability

Atomic model coordinates and cryo-EM density maps for the structures described in this study have been deposited in the Protein Data Bank (PDB) and the Electron Microscopy Data Bank (EMDB) with the following IDs: 8Y8N and EMD-39052 for AQP3 in DDM micelles; 8Y8O and EMD-39053 for AQP3 in POPC nanodiscs; 8Y8S and EMD-39057 for AQP3 in DMPC nanodiscs; 8Y8P and EMD-39054 for AQP3 Y212F in POPC nanodiscs; 8Y8Q and EMD-39055 for AQP3 Y212T in POPC nanodiscs; 8Y8R and EMD-39056 for AQP3 Y212T in DDM micelles; 8Y8V and EMD-39060 for AQP7 in POPC nanodiscs; EMD-39061 for GlpF in DDM micelles; 8Y8W and EMD-39062 for GlpF in POPC nanodiscs; and 8Y8X and EMD-39063 for GlpF ΔP177 in POPC nanodiscs. The initial coordinates, simulation input files, and final output trajectory files of MD simulations have been submitted to the Biological Structure Model Archive (BSM-Arc) under BSM-ID BSM00076 [https://bsma.pdbj.org/entry/76]. Source data are provided with this paper.

References

1. Agre, P. et al. Aquaporin water channels—from atomic structure to clinical medicine. *J. Physiol.* **542**, 3–16 (2002).
2. King, L. S., Kozono, D. & Agre, P. From structure to disease: the evolving tale of aquaporin biology. *Nat. Rev. Mol. Cell Biol.* **5**, 687–698 (2004).
3. Verkman, A. S., Anderson, M. O. & Papadopoulos, M. C. Aquaporins: important but elusive drug targets. *Nat. Rev. Drug Discov.* **13**, 259–277 (2014).
4. Salman, M. M., Kitchen, P., Yool, A. J. & Bill, R. M. Recent breakthroughs and future directions in drugging aquaporins. *Trends Pharmacol. Sci.* **43**, 30–42 (2022).
5. Gonen, T. & Walz, T. The structure of aquaporins. *Q. Rev. Biophys.* **39**, 361–396 (2006).
6. Kreida, S. & Törnroth-Horsefield, S. Structural insights into aquaporin selectivity and regulation. *Curr. Opin. Struct. Biol.* **33**, 126–134 (2015).
7. Nesverova, V. & Törnroth-Horsefield, S. Phosphorylation-dependent regulation of mammalian aquaporins. *Cells* **8**, 82 (2019).
8. Törnroth-Horsefield, S. et al. Insight into the mammalian aquaporin interactome. *Int. J. Mol. Sci.* **23**, 9615 (2022).
9. Murata, K. et al. Structural determinants of water permeation through aquaporin-1. *Nature* **407**, 599–605 (2000).
10. Fu, D. et al. Structure of a glycerol-conducting channel and the basis for its selectivity. *Science* **290**, 481–486 (2000).
11. Sui, H., Han, B. G., Lee, J. K., Walian, P. & Jap, B. K. Structural basis of water-specific transport through the AQP1 water channel. *Nature* **414**, 872–878 (2001).
12. de Groot, B. L. & Grubmüller, H. Water permeation across biological membranes: mechanism and dynamics of aquaporin-1 and GlpF. *Science* **294**, 2353–2357 (2001).
13. Kitchen, P. et al. Water channel pore size determines exclusion properties but not solute selectivity. *Sci. Rep.* **9**, 20369 (2019).
14. Wang, Y., Schulten, K. & Tajkhorshid, E. What makes an aquaporin a glycerol channel? A comparative study of AqpZ and GlpF. *Structure* **13**, 1107–1118 (2005).
15. Hub, J. S., Grubmüller, H. & de Groot, B. L. Dynamics and energetics of permeation through aquaporins. What do we learn from molecular dynamics simulations? *Handb. Exp. Pharmacol.* **190**, 57–76 (2009).
16. Beitz, E. et al. In vitro analysis and modification of aquaporin pore selectivity. *Handb. Exp. Pharmacol.* **190**, 77–92 (2009).
17. Savage, D. F. et al. Structural context shapes the aquaporin selectivity filter. *Proc. Natl. Acad. Sci. USA* **107**, 17164–17169 (2010).
18. de Groot, B. L. & Grubmüller, H. The dynamics and energetics of water permeation and proton exclusion in aquaporins. *Curr. Opin. Struct. Biol.* **15**, 176–183 (2005).
19. Roux, B. & Schulten, K. Computational studies of membrane channels. *Structure* **12**, 1343–1351 (2004).
20. Kosinska Eriksson, U. et al. Subangstrom resolution X-ray structure details aquaporin-water interactions. *Science* **340**, 1346–1349 (2013).
21. Tajkhorshid, E. et al. Control of the selectivity of the aquaporin water channel family by global orientational tuning. *Science* **296**, 525–530 (2002).
22. Walz, T., Fujiyoshi, Y. & Engel, A. The AQP structure and functional implications. *Handb. Exp. Pharmacol.* **190**, 31–56 (2009).
23. Tani, K. & Fujiyoshi, Y. Water channel structures analysed by electron crystallography. *Biochim. Biophys. Acta.* **1840**, 1605–1613 (2014).
24. Kamegawa, A. et al. Structural analysis of the water channel AQP2 by single-particle cryo-EM. *J. Struct. Biol.* **215**, 107984 (2023).
25. de Maré, S. W., Venskutonytė, R., Eltschkner, S., de Groot, B. L. & Lindkvist-Petersson, K. Structural basis for glycerol efflux and selectivity of human aquaporin 7. *Structure* **28**, 215–222 (2020).
26. Moss, F. J. et al. Aquaporin-7: a dynamic aquaglyceroporin with greater water and glycerol permeability than its bacterial homolog GlpF. *Front. Physiol.* **11**, 728 (2020).
27. Zhang, L. et al. The structural basis for glycerol permeation by human AQP7. *Sci. Bull.* **66**, 1550–1558 (2021).
28. Huang, P. et al. Cryo-EM structure supports a role of AQP7 as a junction protein. *Nat. Commun.* **14**, 600 (2023).
29. Gotfryd, K. et al. Human adipose glycerol flux is regulated by a pH gate in AQP10. *Nat. Commun.* **9**, 4749 (2018).
30. Martins, A. P. et al. Targeting aquaporin function: potent inhibition of aquaglyceroporin-3 by a gold-based compound. *PLoS One* **7**, e37435 (2012).
31. Spinello, A., de Almeida, A., Casini, A. & Barone, G. The inhibition of glycerol permeation through aquaglyceroporin-3 induced by mercury(II): a molecular dynamics study. *J. Inorg. Biochem.* **160**, 78–84 (2016).
32. Rodriguez, R. A., Liang, H., Chen, L. Y., Plascencia-Villa, G. & Perry, G. Single-channel permeability and glycerol affinity of human aquaglyceroporin AQP3. *Biochim. Biophys. Acta Biomembr.* **1861**, 768–775 (2019).
33. Yadav, D. K., Kumar, S., Choi, E. H., Chaudhary, S. & Kim, M. H. Computational modeling on aquaporin-3 as skin cancer target: a virtual screening study. *Front. Chem.* **8**, 250 (2020).
34. Notti, R. Q. & Walz, T. Native-like environments afford novel mechanistic insights into membrane proteins. *Trends Biochem. Sci.* **47**, 561–569 (2022).
35. Törnroth-Horsefield, S. et al. Structural mechanism of plant aquaporin gating. *Nature* **439**, 688–694 (2006).
36. van den Berg, B. et al. Structural basis for silicic acid uptake by higher plants. *J. Mol. Biol.* **433**, 167226 (2021).

37. Saitoh, Y. & Suga, M. Structure and function of a silicic acid channel Lsi1. *Front. Plant Sci.* **13**, 982068 (2022).
38. Törnroth-Horsefield, S., Hedfalk, K., Fischer, G., Lindkvist-Petersson, K. & Neutze, R. Structural insights into eukaryotic aquaporin regulation. *FEBS Lett.* **584**, 2580–2588 (2010).
39. Frick, A., Järvå, M. & Törnroth-Horsefield, S. Structural basis for pH gating of plant aquaporins. *FEBS Lett.* **587**, 989–993 (2013).
40. Fischer, G. et al. Crystal structure of a yeast aquaporin at 1.15 Å reveals a novel gating mechanism. *PLoS Biol.* **7**, e1000130 (2009).
41. Zeng, J. et al. High-resolution structure of a fish aquaporin reveals a novel extracellular fold. *Life Sci. Alliance* **5**, e202201491 (2022).
42. Gonen, T., Sliz, P., Kistler, J., Cheng, Y. & Walz, T. Aquaporin-0 membrane junctions reveal the structure of a closed water pore. *Nature* **429**, 193–197 (2004).
43. Gonen, T. et al. Lipid-protein interactions in double-layered two-dimensional AQP0 crystals. *Nature* **438**, 633–638 (2005).
44. Bollag, W. B., Aitkens, L., White, J. & Hyndman, K. A. Aquaporin-3 in the epidermis: more than skin deep. *Am. J. Physiol. Cell Physiol.* **318**, C1144–C1153 (2020).
45. Hara-Chikuma, M. & Verkman, A. S. Roles of aquaporin-3 in the epidermis. *J. Investig. Dermatol.* **128**, 2145–2151 (2008).
46. Marlar, S., Jensen, H. H., Login, F. H. & Nejsum, L. N. Aquaporin-3 in cancer. *Int. J. Mol. Sci.* **18**, 2106 (2017).
47. Denisov, I. G., Grinkova, Y. V., Lazarides, A. A. & Sligar, S. G. Directed self-assembly of monodisperse phospholipid bilayer nanodiscs with controlled size. *J. Am. Chem. Soc.* **126**, 3477–3487 (2004).
48. Denisov, I. G., Baas, B. J., Grinkova, Y. V. & Sligar, S. G. Cooperativity in cytochrome P450 3A4: linkages in substrate binding, spin state, uncoupling, and product formation. *J. Biol. Chem.* **282**, 7066–7076 (2007).
49. Mastronarde, D. N. Automated electron microscope tomography using robust prediction of specimen movements. *J. Struct. Biol.* **152**, 36–51 (2005).
50. Kimanius, D., Dong, L., Sharov, G., Nakane, T. & Scheres, S. H. W. New tools for automated cryo-EM single-particle analysis in RELION-4.0. *Biochem. J.* **478**, 4169–4185 (2021).
51. Scheres, S. H. W. RELION: implementation of a Bayesian approach to cryo-EM structure determination. *J. Struct. Biol.* **180**, 519–530 (2012).
52. Punjani, A., Rubinstein, J. L., Fleet, D. J. & Brubaker, M. A. cryoSPARC: algorithms for rapid unsupervised cryo-EM structure determination. *Nat. Methods* **14**, 290–296 (2017).
53. Zheng, S. Q. et al. MotionCor2: anisotropic correction of beam-induced motion for improved cryo-electron microscopy. *Nat. Methods* **14**, 331–332 (2017).
54. Punjani, A., Zhang, H. & Fleet, D. J. Non-uniform refinement: adaptive regularization improves single-particle cryo-EM reconstruction. *Nat. Methods* **17**, 1214–1221 (2020).
55. Zivanov, J., Nakane, T. & Scheres, S. H. W. A Bayesian approach to beam-induced motion correction in cryo-EM single-particle analysis. *IUCrJ* **6**, 5–17 (2019).
56. Rosenthal, P. B. & Henderson, R. Optimal determination of particle orientation, absolute hand, and contrast loss in single-particle electron cryomicroscopy. *J. Mol. Biol.* **333**, 721–745 (2003).
57. Jumper, J. et al. Highly accurate protein structure prediction with AlphaFold. *Nature* **596**, 583–589 (2021).
58. Tunyasuvunakool, K. et al. Highly accurate protein structure prediction for the human proteome. *Nature* **596**, 590–596 (2021).
59. Yamashita, K., Palmer, C. M., Burnley, T. & Murshudov, G. N. Cryo-EM single-particle structure refinement and map calculation using *Servalcat*. *Acta Crystallogr. D Struct. Biol.* **77**, 1282–1291 (2021).
60. Emsley, P., Lohkamp, B., Scott, W. G. & Cowtan, K. Features and development of *Coot*. *Acta Crystallogr. D Biol. Crystallogr.* **66**, 486–501 (2010).
61. Adams, P. D. et al. *PHENIX*: a comprehensive Python-based system for macromolecular structure solution. *Acta Crystallogr. D Biol. Crystallogr.* **66**, 213–221 (2010).
62. Williams, C. J. et al. MolProbity: more and better reference data for improved all-atom structure validation. *Protein Sci.* **27**, 293–315 (2018).
63. Goddard, T. D. et al. UCSF ChimeraX: meeting modern challenges in visualization and analysis. *Protein Sci.* **27**, 14–25 (2018).
64. Pravda, L. et al. MOLEonline: a web-based tool for analyzing channels, tunnels and pores (2018 update). *Nucleic Acids Res.* **46**, W368–W373 (2018).
65. Müller-Lucks, A. et al. Preparative scale production and functional reconstitution of a human aquaglyceroporin (AQP3) using a cell free expression system. *N. Biotechnol.* **30**, 545–551 (2013).
66. Olsson, M. H. M., Søndergaard, C. R., Rostkowski, M. & Jensen, J. H. PROPKA3: consistent treatment of internal and surface residues in empirical p*K*a predictions. *J. Chem. Theory Comput.* **7**, 525–537 (2011).
67. Jo, S., Kim, T., Iyer, V. G. & Im, W. CHARMM-GUI: a web-based graphical user interface for CHARMM. *J. Comput. Chem.* **29**, 1859–1865 (2008).
68. Brooks, B. R. et al. CHARMM: the biomolecular simulation program. *J. Comput. Chem.* **30**, 1545–1614 (2009).
69. Lee, J. et al. CHARMM-GUI input generator for NAMD, GROMACS, AMBER, OpenMM, and CHARMM/OpenMM simulations using the CHARMM36 additive force field. *J. Chem. Theory Comput.* **12**, 405–413 (2016).
70. Wu, E. L. et al. CHARMM-GUI membrane builder toward realistic biological membrane simulations. *J. Comput. Chem.* **35**, 1997–2004 (2014).
71. Jo, S., Lim, J. B., Klauda, J. B. & Im, W. CHARMM-GUI membrane builder for mixed bilayers and its application to yeast membranes. *Biophys. J.* **97**, 50–58 (2009).
72. Jo, S., Kim, T. & Im, W. Automated builder and database of protein/membrane complexes for molecular dynamics simulations. *PLoS ONE* **2**, e880 (2007).
73. Lee, J. et al. CHARMM-GUI membrane builder for complex biological membrane simulations with glycolipids and lipoglycans. *J. Chem. Theory Comput.* **15**, 775–786 (2019).
74. Park, S., Choi, Y. K., Kim, S., Lee, J. & Im, W. CHARMM-GUI membrane builder for lipid nanoparticles with ionizable cationic lipids and PEGylated lipids. *J. Chem. Inf. Model.* **61**, 5192–5202 (2021).
75. Cheng, X., Jo, S., Lee, H. S., Klauda, J. B. & Im, W. CHARMM-GUI micelle builder for pure/mixed micelle and protein/micelle complex systems. *J. Chem. Inf. Model.* **53**, 2171–2180 (2013).
76. Lomize, M. A., Pogozheva, I. D., Joo, H., Mosberg, H. I. & Lomize, A. L. OPM database and PPM web server: resources for positioning of proteins in membranes. *Nucleic Acids Res.* **40**, D370–D376 (2012).
77. Abrahama, M. J. et al. GROMACS: high performance molecular simulations through multi-level parallelism from laptops to supercomputers. *Software X* **1–2**, 19–25 (2015).
78. Huang, J. et al. CHARMM36m: an improved force field for folded and intrinsically disordered proteins. *Nat. Methods* **14**, 71–73 (2017).
79. Guvench, O. et al. CHARMM additive all-atom force field for carbohydrate derivatives and their utility in polysaccharide and carbohydrate-protein modeling. *J. Chem. Theory Comput.* **7**, 3162–3180 (2011).
80. Mallajosyula, S. S., Guvench, O., Hatcher, E. & MacKerell, A. D. Jr. CHARMM additive all-atom force field for phosphate and sulfate linked to carbohydrates. *J. Chem. Theory Comput.* **8**, 759–776 (2012).
81. Raman, E. P., Guvench, O. & MacKerell, A. D. Jr. CHARMM additive all-atom force field for glycosidic linkages in carbohydrates involving furanoses. *J. Phys. Chem. B* **114**, 12981–12994 (2010).

82. Guvench, O., Hatcher, E. R., Venable, R. M., Pastor, R. W. & MacKerell, A. D. Jr. Additive empirical CHARMM force field for glycosyl linked hexopyranoses. *J. Chem. Theory Comput.* **5**, 2353–2370 (2009).
83. Klauda, J. B. et al. Update of the CHARMM all-atom additive force field for lipids: validation on six lipid types. *J. Phys. Chem. B* **114**, 7830–7843 (2010).
84. Jorgensen, W. L., Chandrasekhar, J., Madura, J. D., Impey, R. W. & Klein, M. L. Comparison of simple potential functions for simulating liquid water. *J. Chem. Phys.* **79**, 926–935 (1983).
85. Hess, B. P-LINCS: a parallel linear constraint solver for molecular simulation. *J. Chem. Theory Comput.* **4**, 116–122 (2008).
86. Essmann, U. et al. A smooth particle mesh Ewald method. *J. Chem. Phys.* **103**, 8577–8593 (1995).
87. Berendsen, H. J. C., Postma, J. P. M., van Gunsteren, W. F., DiNola, A. & Haak, J. R. Molecular dynamics with coupling to an external bath. *J. Chem. Phys.* **81**, 3684–3690 (1984).
88. Nosé, S. A molecular dynamics method for simulations in the canonical ensemble. *Mol. Phys.* **52**, 255–268 (1984).
89. Hoover, W. G. Canonical dynamics: equilibrium phase-space distributions. *Phys. Rev. A* **31**, 1965–1967 (1985).
90. Parrinello, M. & Rahman, A. Polymorphic transitions in single crystals: a new molecular dynamics method. *J. Appl. Phys.* **52**, 7182–7190 (1981).
91. Nosé, S. & Klein, M. L. Constant pressure molecular dynamics for molecular systems. *Mol. Phys.* **50**, 1055–1076 (1983).
92. Case, D. A. et al. Amber 2022, (University of California, San Francisco, 2022).
93. Humphrey, W., Dalke, A. & Schulten, K. VMD: visual molecular dynamics. *J. Mol. Graph.* **14**, 33–38 (1996).

Acknowledgements

This work was supported by Grants-in-Aid for Scientific Research (A) under Grant Number 20H00451 and the Japan Agency for Medical Research and Development (AMED) under Grant Number JP21ae0121028 for Y.F. We thank former members of the Y.F. laboratory for the early-stage AQP3 research. This research was supported by Research Support Project for Life Science and Drug Discovery (Basis for Supporting Innovative Drug Discovery and Life Science Research (BINDS)) from AMED under Grant Number JP24ama121023 for M.Ikeguchi.

Author contributions

D.K. performed protein expression and purification of AQP3 and GlpF. A.K. performed protein expression and purification of AQP7. D.K., S.S., A.K., K.N., and H.S. performed cryo-EM data acquisition. D.K. and S.S. processed cryo-EM data and refined structural models with support from H.S. D.K. performed stopped-flow measurements with support from A.K., M. Inoue, T.E., and M.Ikeguchi performed MD simulations. D.K. and M. Inoue prepared the original draft. D.K., M. Inoue, S.S., A.K., H.S., T.E., M. Ikeguchi, and Y.F. wrote the manuscript, which was approved by all authors. Y.F. supervised the overall research.

Competing interests

The authors declare no competing interests.

Additional information

Supplementary information The online version contains supplementary material available at https://doi.org/10.1038/s41467-025-57728-3.

Correspondence and requests for materials should be addressed to Yoshinori Fujiyoshi.

Peer review information *Nature Communications* thanks Douglas J. Tobias and the other, anonymous, reviewer(s) for their contribution to the peer review of this work. A peer review file is available.